10/6-14-95 g.s.D

LBL-36903
UC-400

Lawrence Berkeley Laboratory
UNIVERSITY OF CALIFORNIA

EARTH SCIENCES DIVISION

Predicting the Permeability of Sedimentary Rocks from Microstructure

E.M. Schlueter

January 1995

Prepared for the U.S. Department of Energy under Contract Number DE-AC03-76SF00098

Available to DOE and DOE Contractors
from the Office of Scientific and Technical Information
P.O. Box 62, Oak Ridge, TN 37831
Prices available from (615) 576-8401

Available to the public from the
National Technical Information Service
U.S. Department of Commerce
5285 Port Royal Road, Springfield, VA 22161

Predicting the Permeability of Sedimentary Rocks from Microstructure*

Erika M. Schlueter

(Excerpt from Ph.D. Thesis)

Department of Materials Science and Mineral Engineering
University of California

and

Earth Sciences Division
Lawrence Berkeley Laboratory
University of California
Berkeley, California 94720

January 1995

---

*This research was supported by the U.S. Department of Energy through the Assistant Secretary for Fossil Energy, Bartlesville Project Office, Advanced Extraction Process Technology (AEPT), under contract No. DE-AC22-89BC14475, and by the Director, Office of Energy Research, Office of Basic Energy Sciences, Engineering and Geosciences Division, under Contract No. DE-AC03-76SF00098.

DISCLAIMER

Portions of this document may be illegible in electronic image products. Images are produced from the best available original document.

3 PREDICTING PERMEABILITY OF SEDIMENTARY ROCKS FROM MICROSTRUCTURE

The concept of permeability allows a macroscopic description of the fluid flow phenomena in porous media under a regime of sufficiently low fluid velocities (Scheidegger, 1974). This property is linked to other properties of porous media such as capillary pressure and relative permeability. In order to understand the relationships, one has to understand how all those properties are conditioned by the connectivity and geometrical properties of the pore space. The simplest model that can be constructed is one representing a porous medium by a bundle of straight, parallel cylindrical capillaries of uniform diameter that go from one face of the porous medium to the other. Equations based on this type of 1-D model are called Kozeny-Carman equations. The opposite extreme of this parallel case would be to assume a serial model in which all the pores are connected in series. Obviously, for a natural porous medium, this model is as idealized as the parallel model, and a realistic model lies somewhere between these limits.

In this study, we look at a natural porous material which is defined as a two-phase material in which the interconnected pore space constitutes one phase and the solid matrix the other. A distinctive property of a natural porous medium is the irregular pore-size and pore-shape distributions. We consider here the pore scale and its extention to the laboratory scale which is of the order of tens to thousands times larger. The laboratory samples are considered homogeneous in the sense that the irregular pore structure reproduces itself in the various portions of the sample. In a typical fluid flow laboratory experiment, the rates of flow are measured over areas which intersect many pores. Space-averaged or macroscopic quantities such as permeability are the ones of interest in applications. The main aim of this Chapter is to develop equations relating a macroscopic property such as permeability to rock microstructure. A few methods have been used in the past in order to achieve this (Schlueter, 1995). Two basic averaging approaches have been employed here. In the first one, the discrete approach, a macroscopic variable such as effective conductance is determined as an appropiate mean over a sufficiently large representative elementary volume (r.e.v.) defined through the concept of porosity associated with it. The length scale of the

r.e.v. is larger than the size of a single pore so that it includes a sufficient number of pores to allow the meaningful statistical average required in the continuum concept. It is assumed that results concerning the macroscopic quantities are independent of the size of the r.e.v. In the second one, the statistical approach is related to the uncertainty of the spatial distribution of microscopic quantities such as pore-sizes and pore-shapes. The statistical averaging is carried out over one realization. The actual sample is one of the possible realizations of media of some gross features. But the inference of statistical information about the realization is based on the unique sample. This is possible only under restrictive conditions of statistical homogeneity (stationarity) which are similar in essence to those underlying the concept of r.e.v. As long as we limit ourselves to deriving relationships between space averaged quantities with no special concern as to their fluctuations, the results of the two approaches should be essentially the same.

3.1 Discrete approach to individual conductances

Consider an inhomogeneous, disordered, composite system (conductive/non-conductive) in which one can define locally a given property, e.g., conductance, which can be calculated from the geometry of the conductive element (e.g., the coefficient in Poiseuille's law for cylindrical tubes). This is possible as long as the dimensions of the local elements are large with respect to the scale of the conduction process involved (i.e., as long as the individual pores are wide enough so that fluid flow obeys the macroscopic Navier-Stokes equations, and is not dominated by surface effects). Such a medium can be approximated by a 3-D network with the same topology, in which all the conductances have a single effective value. The effective medium can be defined as one in which the macroscopic conductance is the same as for the heterogeneous system, and therefore the effective conductance can be considered as the mean value controlling the physical property of concern. Since we are concerned with a random medium, it is assued that no spatial correlation exists between the individual conductances. Details of the effective medium theory of solid state physics are given in Section 3.1.1.

For this study, rock cross sections have been prepared for imaging with the scanning electron microscope (SEM). The resulting 2-D SEM photomicrographs have been

employed to infer the hydraulic conductance of the individual pores. We assume that the pores are cylindrical tubes of varying radius, and that they are arranged on a cubic lattice, so that the coordination number of the network is 6. The hydraulic conductance of each tube is estimated from its area and perimeter, using the hydraulic radius approximation and the Hagen-Poiseuille equation. In the section under consideration, the pore cross sections are assumed to be randomly oriented with respect to the directions of the channel axes. The orientation effect has been corrected by means of geometrical and stereological considerations. Account is also taken for possible variation of the cross-sectional area along the length of each tube, e.g., pore necks and bulges. The effective-medium theory of solid-state physics is then used to replace each individual conductance with an effective average conductance. Finally, a unit cubic cell is extended to relate the effective-hydraulic-tube conductances to the continuum values of permeability. Preliminary results, using Berea, Boise, Massilon, and Saint-Gilles sandstone, yield very close agreement between the predicted and measured permeabilities, with essentially no arbitrary parameters in the model.

3.1.1 Effective medium theory

The objective of the effective medium theory (Kirkpatrick, 1973) is to infer an average conductance parameter for heterogeneous disordered media from the statistics of local conducting elements. Consider an inhomogeneous disordered continuous system in which one can define locally the conductance. Such a medium can be approximated by a 3-D network with a regular topology in which each bond is occuppied by a conductance C_i. According to Kirkpatrick (1973) it is possible to build a homogeneous network with the same topology but in which all conductances C_i have a single value C_{eff} which is an effective value controlling the physical property involved. The effective medium is by definition the homogeneous equivalent network for which the macroscopic conductance is the same as for the heterogeneous system. The idea then, is to represent the average effects of the random conductors by a homogeneous effective medium in which the total field inside is equal to the external field. As a criterion to fix C_{eff} it is required that the incremental voltages induced, where individual conductances C_i are replaced by C_{eff} in this medium, should average to zero.

The distribution of potentials in a random resistor network to which a voltage has been applied along one axis may be regarded as due to both (1) an external field which increases the voltage by a constant amount per row of nodes, and (2) a local fluctuating field whose average over a sufficiently large region is zero.

3.1.1.1 *Uniform field solution (external field)*

By introducing a regular cubic mesh of points r_i with spacing $\triangle r$ (Figure 3.1), and applying the principle of conservation of charge, one obtains a system of linear equations for the voltages $V_i = V_{r_i}$.

At point i,

$$\sum_j C_{ij}(V_i - V_j) = 0 \,, \tag{1}$$

where j is summed over all neighboring points.

Replacing the conductance C_{ij} with a constant effective conductance C_{eff}, gives at point A (refer to Figure 3.1)

$$C_{eff}([V + 2V_{eff}]4 - [V + 3V_{eff} + V + V_{eff} + V + 2V_{eff} + V + 2V_{eff}]) = 0 \,, \tag{2}$$

where all conductances C_{eff} have associated with them $\triangle V = V_{eff}$ per row.

3.1.1.2 *Fluctuating field solution (local field)*

To find a mathematical expression for the effective conductance, a classical self-consistent method can be employed in which a single conductance C_o is embedded in the homogeneous medium of similar topology. The inclusion of C_o in the effective medium disturbs locally the uniform solution for the field but the deviation is easily calculated since the effective network is homogeneous.

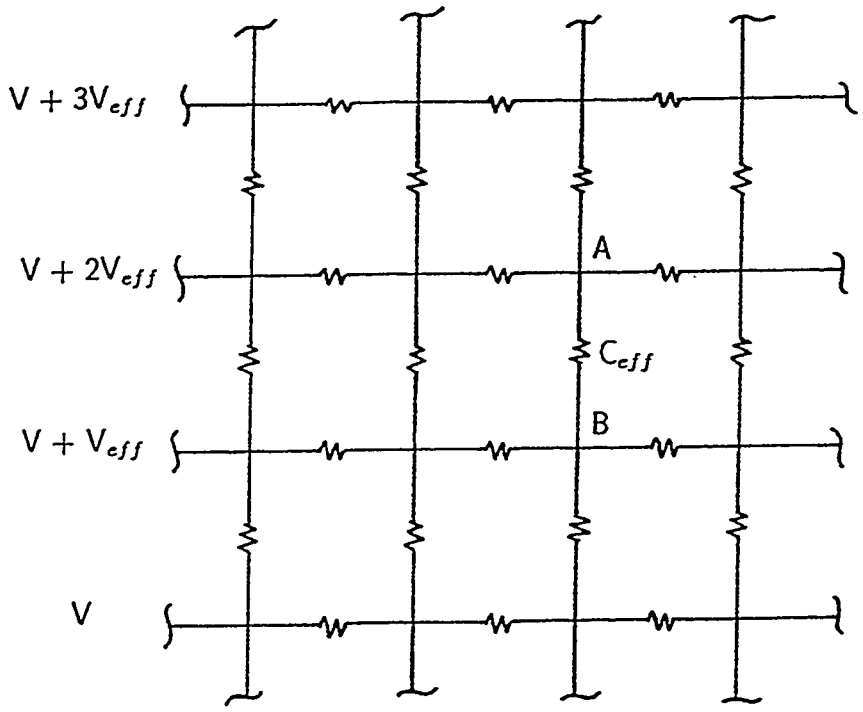

FIG. 3.1: Construction used in calculating the uniform field solution, in which the voltages increase by a constant amount, V_m, per row.

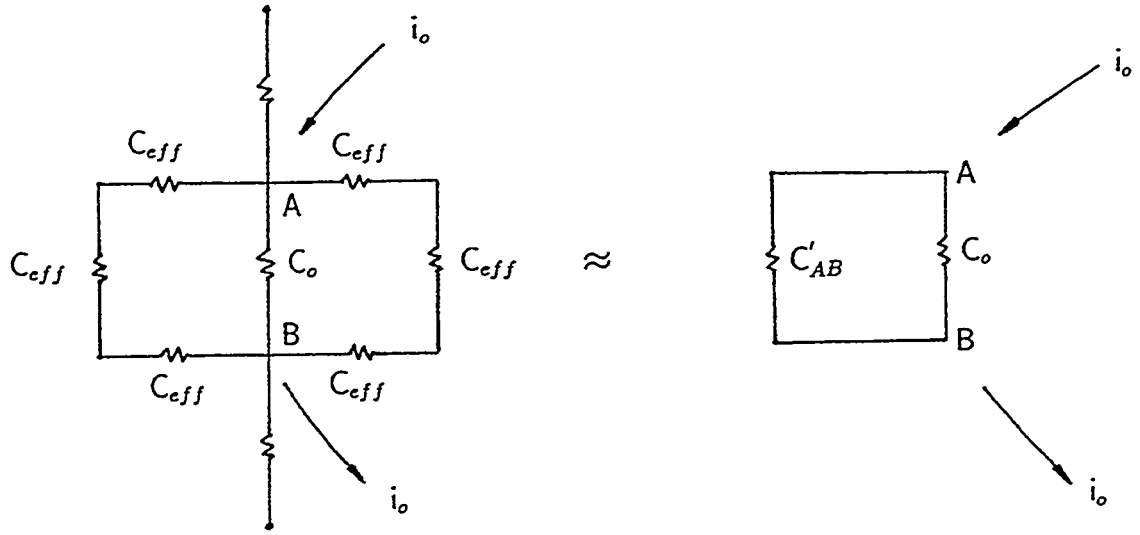

FIG. 3.2: Construction used in calculating the voltage induced across one conductance, C_o, surrounded by a uniform medium (after Kirkpatrick, 1973).

Consider one conductance having the value C_o surrounded by an otherwise uniform effective medium. The solution of the network Eq. (1) in the presence of C_o can be constructed by superposition (Figure 3.2). Far from C_o the field is uniform. To the uniform field solution given by Eq. (2), we add the effects of a fictitious current i_o introduced at A and extracted at B. Since the uniform solution fails to satisfy current conservation at A and B, the magnitude of i_o is chosen to correct for this.

At A,

$$V_{eff}(C_{eff} - C_o) = i_o \, . \tag{3}$$

The extra voltage, V_o, induced between A and B, is given by the conductance C'_{AB} of the network between points A and B when the perturbation is absent, i.e., when $C_o - C_{eff} = 0$:

$$V_o = \frac{i_o}{C_o + C'_{AB}} \, . \tag{4}$$

The current flowing through each of the z equivalent nodes at the point where the current enters is i_o/z so that a total current of $2i_o/z$ flows through the path AB. We then calculate the voltage developed across AB, the conductance across AB, $C_{AB} = (z/2)C_{eff}$, and $C'_{AB} = (z/2)C_{eff} - C_{eff}$.

Thus we can write

$$V_o = \frac{V_{eff}(C_{eff} - C_o)}{C_o + [z/2 - 1]C_{eff}} \, , \tag{5}$$

valid both in 2-D and 3-D.

The requirement that the average of V_o vanishes gives

$$\left\langle \frac{C_{eff} - C_i}{[(z/2) - 1]C_{eff} + C_i} \right\rangle = \sum_{i=1}^{N} \frac{C_{eff} - C_i}{[(z/2) - 1]C_{eff} + C_i} = 0 \, , \tag{6}$$

where the sum is taken over all N individual conductors.

Upper and lower bounds on the effective conductivity are found from the two limiting cases $z = 2$ and $z = \infty$. For $z = 2$, Eq. (6) can be solved for

$$C_{eff} = \frac{N}{\sum_{i=1}^{N} \frac{1}{C_i}}, \tag{7}$$

whereas for $z = \infty$, Eq. (6) can be solved for

$$C_{eff} = \frac{\sum_{i=1}^{N} C_i}{N}. \tag{8}$$

When the coordination number is 2, the tubes are arranged in series, and the effective conductance reaches its lowest possible value. On the other hand, when the coordination number is ∞, the tubes are arranged in parallel, and the effective conductance reaches its maximum value. The limiting values of both the effective conductance and the coordination number correspond to one-dimensional arrangements of the tubes. For a coordination number other than $z = 2$ or $z = \infty$, Eq. (6) must be solved numerically to find the effective conductance, given the individual conductances (See Code Listing 3.1).

The effective medium theory is expected to work best when spatial fluctuations of hydraulic (or current) flux are small in a relative scale. Our laboratory imbibition experiments in Berea sandstone, in combination with SEM analysis of the pore space, indicate that the distribution of pores and throats controlling permeability is narrow. Consequently, the effective medium theory is expected to, and does, give very good results in Berea sandstone. The effective medium theory coupled with a network of resistors has been used by Koplik et al. (1984) to predict permeability of Massilon sandstone, although the predicted value was ten times higher than that measured. Doyen (1988) calculated the transport properties of Fontainebleau sandstone, and predicted permeability within a factor of three of the measured value. These models do not account for the fact that the 2-D section under consideration slices each pore at a random angle to its axis or for the variation of the cross-sectional area along the length of each tube, both of which are significant effects. These effects are discussed below in sections 3.1.4 and 3.1.5, respectively.

3.1.2 Method of analysis

Figures 3.3 and 3.4, stereo SEM photomicrographs of pore casts of Berea sandstone and Saint-Gilles sandstone, respectively, reveal that the pore space is comprised of a three-dimensional network of irregularly shaped pores. Although an exact description of key pore space morphological characteristics is rather complex, it is possible to isolate three main features:

1. Multiple connectivity of the pore segments;
2. Converging-diverging cross sections of pores;
3. Roughness and irregularity of pore walls.

Since the actual rock geometry is too complex for any quantitative study, we have replaced it by a standard model geometry that preserves the main observed morphological features.

For the purposes of developing a network model for permeability, we need to know the volumetric flow through each pore. According to the Hagen-Poiseuille equation, the volumetric flux of fluid through a cylindrical pore of constant radius r is

$$q = \frac{\pi r^4}{8\mu} \nabla p \,, \tag{9}$$

where μ is the absolute viscosity, and ∇p is the pressure gradient. We now use the hydraulic radius concept to rewrite Eq. (9) in a form that is applicable to non-circular pores (See Section 3.1.3 for details).

The hydraulic radius R_H of the tube is defined as

$$R_H \equiv \frac{area}{wetted - perimeter} \,. \tag{10}$$

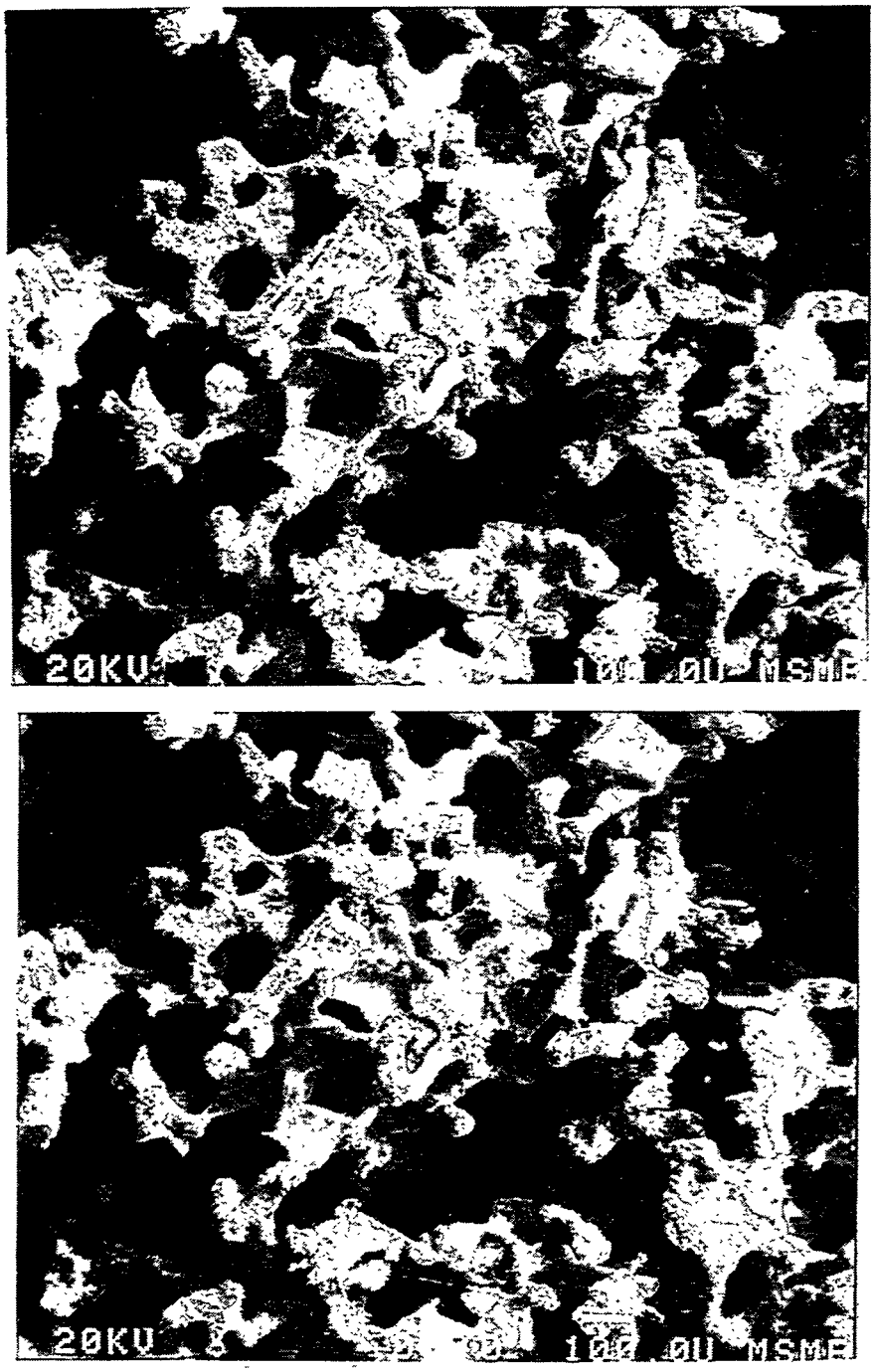

FIG. 3.3: Stereo SEM photomicrographs of a Berea sandstone pore cast. The pore space is partially impregnated with Wood's metal alloy and the quartz grains removed by hydrofluoric acid.

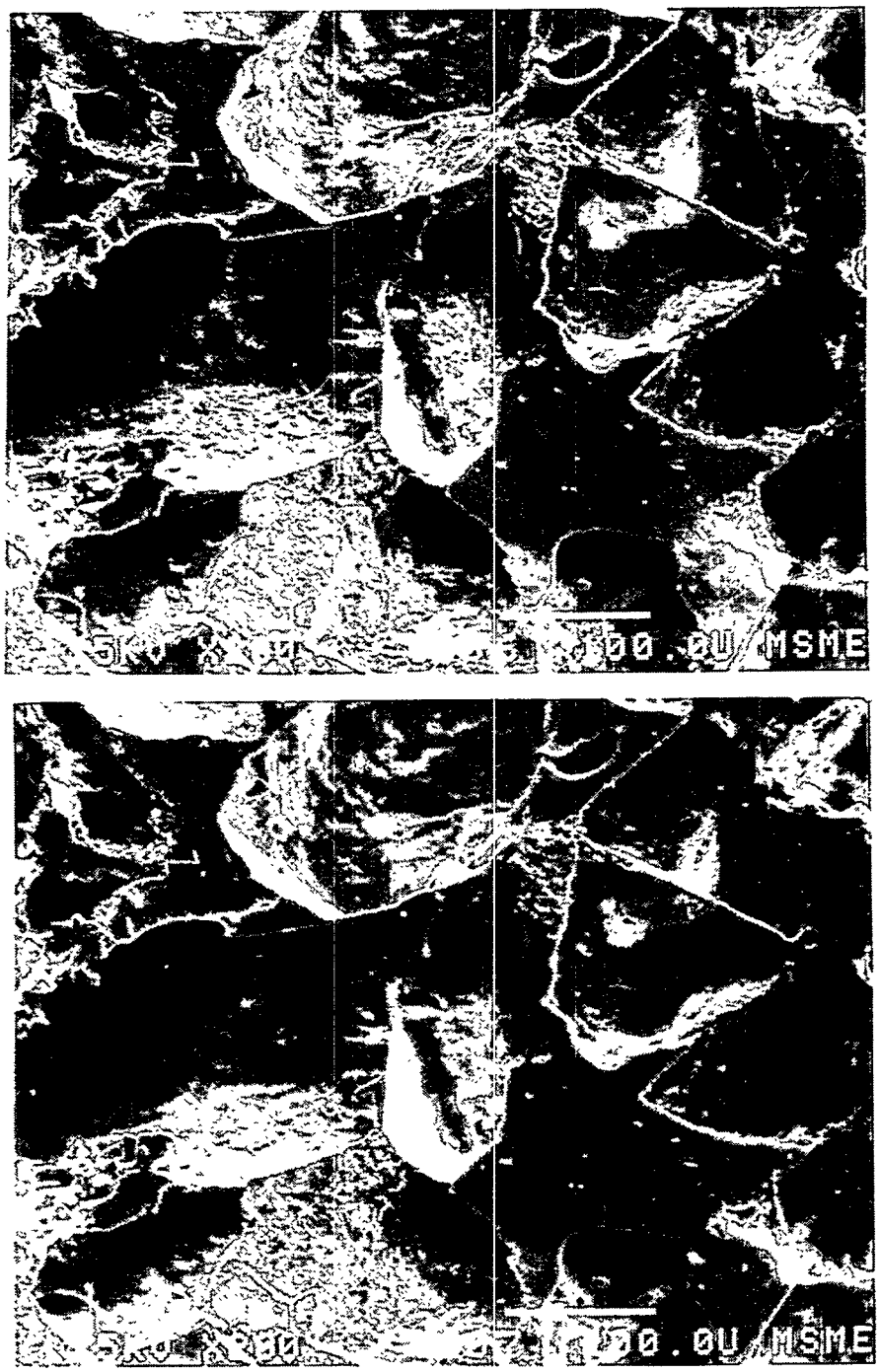

FIG. 3.4: Stereo SEM photomicrographs of a Saint-Gilles sandstone pore cast. The pore space is partially impregnated with epoxy and the quartz grains removed by hydrofluoric acid.

Using Eq. (10), we can rewrite Eq. (9) in terms of the hydraulic radius as

$$q = \frac{R_H^2 A}{2\mu} \nabla p \,, \tag{11}$$

where A is the area of the tube.

The conductance of a tube of area A and length l is given by $\sigma A/l$, where σ is the conductivity. The hydraulic conductance per unit length of each tube is therefore (aside from a length factor which eventually cancels out of the calculations) given by

$$C_i = \frac{R_H^2}{2} A \,. \tag{12}$$

The constant length of each tube assigned to all tubes in the model is assumed to be of the order of the correlation length characterizing the fluctuations of the channel cross-sectional dimensions. Measurements of two-point correlation functions (Berryman and Blair, 1986) show that the correlation length is of the order of the size of the grains in sandstone. Thus, the pore length can be assumed to be equal to the grain diameter. However, as mentioned earlier, the length does not need to appear explicitly in Eq. (6) where all conductances are proportional to L^{-1}. The local conductive elements have been obtained from 2-D SEM photomicrographs of rock sections. Figures 3.5a, 3.6a, 3.8a, and 3.9a show 2-D SEM photomicrographs of Berea sandstone (Sections B and T), Boise sandstone, and Saint-Gilles sandstone, respectively. Typical pore-space contours obtained from 2-D SEM photomicrographs of Berea, Massilon, Boise, and Saint-Gilles sandstones are shown in Figures 3.5b, 3.6b, 3.7, 3.8b, and 3.9b, respectively. The pore space contours are employed to estimate the area, perimeter, and individual conductance of each tube of varying radius using the hydraulic radius approximation and Poiseuille's law.

The basic method to calculate individual pore areas, perimeters, and hydraulic radii involves counting size and perimeter grid (or pixel) units for every feature in a standard scanning electron micrograph of some fixed magnification. The field imaged by each micrograph must contain a large enough number of pores to assure a statistically representative sample; we have found that 30-40 pores suffice for this purpose. The analysis was carried out using both a manual and an automated im-

age analysis procedure to verify the accuracy of the manual technique. The manual technique involved overlaying a square grid, with grid size of 2.54 mm, and visually counting the number of grid blocks occupied by the area of each pore, as well as the number of grid blocks that the perimeter passes through. Digital images with typical image sizes of 482 $\times$ 640 pixels, and 8 bits per pixel to quantify the darkness level, were used for studying the accuracy of the manual technique. The image analysis program sets a threshold level of darkness to distinguish between the pore contours and mineral grains. The digitized thin sections of Berea, Massilon, Boise, and Saint-Gilles sandstones (Figures 3.5b, 3.6b, 3.7, 3.8b, and 3.9b, respectively) then show pore space in white, and mineral grains in black. This method was used to estimate the area, perimeter, hydraulic radii, and hydraulic conductance of individual pores for each rock. Results for Berea (Sections B and T), Massilon, Boise, and Saint-Gilles sandstones are presented in Tables 3.1 to 3.5, respectively.

In the next section, the effect of pore shape on permeability will be studied: (1) to compare the exact permeabilities of various polygonal-shaped pores with the hydraulic-radius predictions, and (2) to calculate the error involved in using the hydraulic radius approximation and Poiseuille's law to estimate the individual pore conductances.

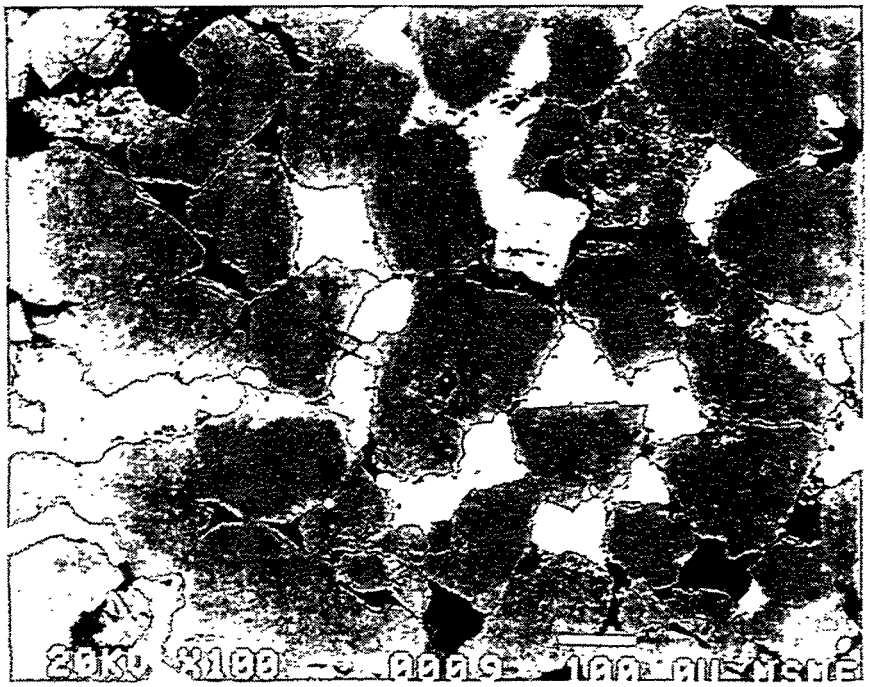

FIG. 3.5a: Typical SEM photomicrograph of Berea sandstone (Section B). The rock is composed mainly of quartz grains (dark gray), feldspar grains (medium gray), and products of grain dissolution (light gray). The pore space is impregnated with Wood's metal alloy (white), and epoxy (black). Actual width of field is about 1 mm.

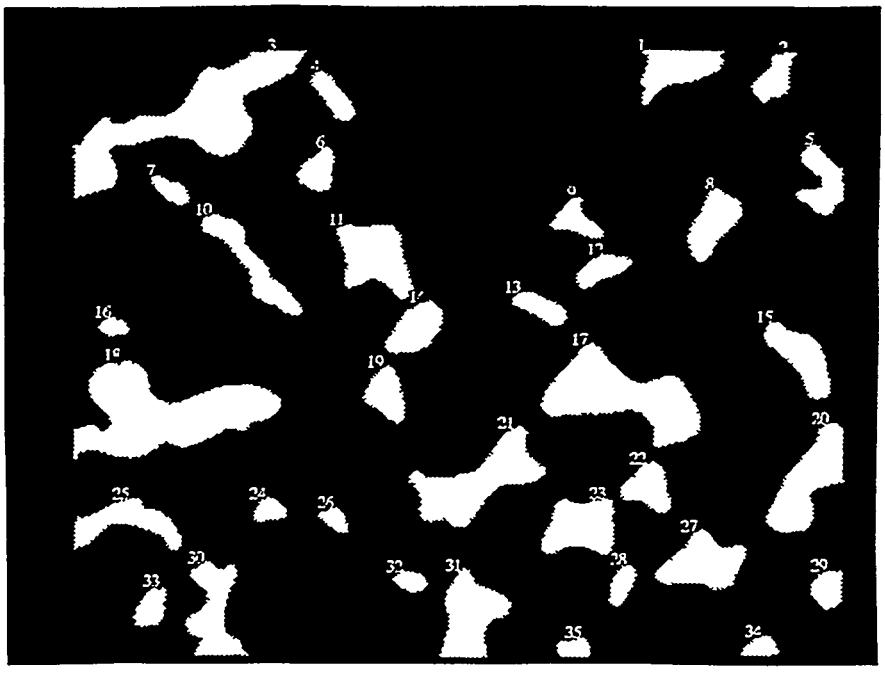

FIG. 3.5b: Pore-space contours obtained from image analysis of the photomicrograph of Berea sandstone (Section B) shown in Fig. 3.5a. The width of field is about 1 mm.

TABLE 3.1: Conductance data - Berea sandstone SEM section B.

N_i	A_i (units)	P_i (units)	A_i $\times 10^{-10}(\mathrm{m}^2)$	P_i $\times 10^{-5}$ (m)	R_{H_i} $\times 10^{-5}$(m)	C_i $\times 10^{-20}$ (m^4)
1	27	34	168.75	85.00	1.99	332.61
2	3	8	18.75	17.50	1.07	10.76
3	7	9	43.75	22.50	1.94	82.73
4	4	7	25.00	17.50	1.43	25.53
5	2	5	12.50	12.50	1.00	6.25
6	3	6	18.75	15.00	1.25	14.66
7	6	12	37.50	30.00	1.25	29.33
8	8	16	50.00	40.00	1.25	39.10
9	13	15	81.25	37.50	2.17	190.69
10	3	8	18.75	20.00	0.94	8.25
11	5	10	31.25	25.00	1.25	24.44
12	3	7	18.25	17.50	1.07	10.76
13	5	9	31.25	22.50	0.94	13.94
14	3	7	18.75	17.50	1.07	10.76
15	1	4	6.25	10.00	0.63	1.23
16	34	24	212.50	60.00	3.54	1332.80
17	4	8	25.00	20.00	1.25	19.55
18	24	24	150.00	60.00	2.50	468.75
19	7	12	43.75	30.00	1.46	46.55
20	7	14	43.75	35.00	1.25	34.21
21	2	5	12.50	12.50	1.00	6.25
22	2	5	12.50	12.50	1.00	6.25
23	18	21	112.50	52.50	2.14	258.30
24	4	9	25.00	22.50	1.11	15.45
25	10	14	62.50	35.00	1.79	99.69
26	10	13	62.50	32.50	1.92	115.56
27	2	6	12.50	15.00	0.83	4.34
28	9	16	56.20	40.00	1.41	55.58
29	1	4	6.25	10.00	0.63	1.23
30	12	10	75.00	25.00	3.00	337.50
31	2	5	12.50	12.50	1.00	6.25
32	8	13	50.00	32.50	1.54	59.20
33	2	4	12.50	10.00	1.25	9.78
34	1	3	6.25	7.50	0.83	2.14
35	2	3	12.50	7.50	1.67	17.36

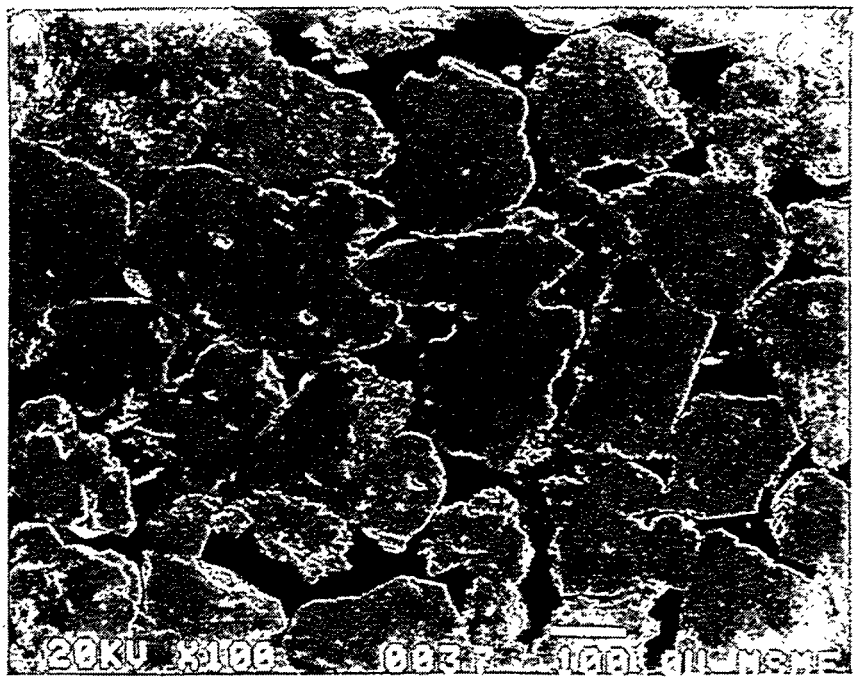

FIG. 3.6a: Typical SEM photomicrograph of Berea sandstone (Section T). The rock is composed of quartz grains (dark gray). The pore space is impregnated with epoxy (black). Actual width of field is about 1 mm.

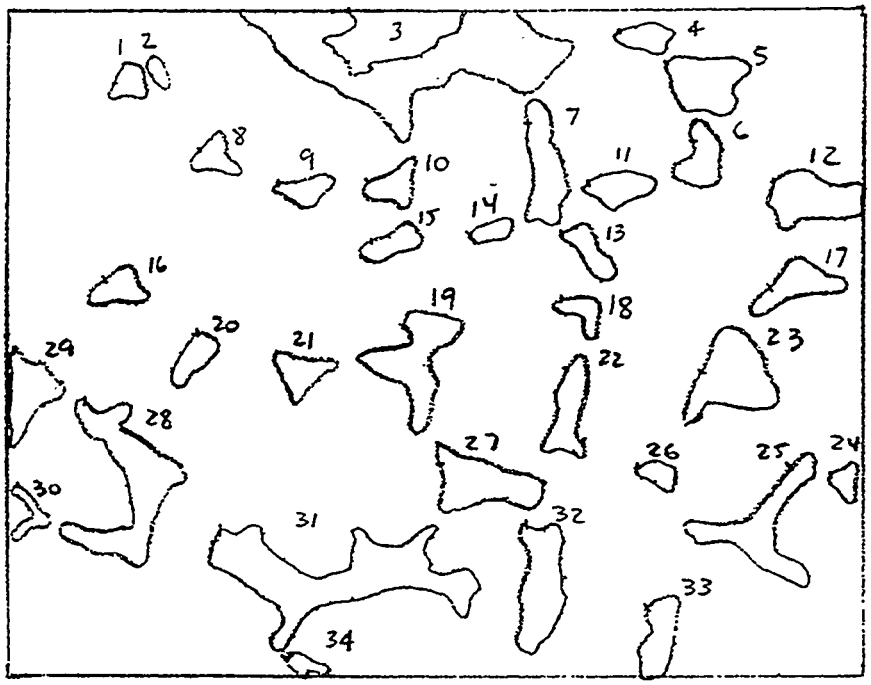

FIG. 3.6b: Pore-space contours obtained from computerized image analysis of the photomicrograph of Berea sandstone (Section T) shown in Fig. 3.6a. The width of field is about 1 mm.

TABLE 3.2: Conductance data - Berea sandstone SEM section T.

N_i	A_i (units)	P_i (units)	A_i $\times 10^{-10}(\mathrm{m}^2)$	P_i $\times 10^{-5}$ (m)	R_{H_i} $\times 10^{-5}$(m)	C_i $\times 10^{-20}(\mathrm{m}^4)$
1	3	7	18.75	17.50	1.07	10.76
2	1.5	6	9.38	15.00	0.63	1.83
3	45.5	56	284.38	140.00	2.03	586.67
4	3.5	9	21.88	22.50	0.97	10.34
5	9.5	15	59.38	37.50	1.58	74.42
6	5	12	31.25	30.00	1.04	16.96
7	9.5	18	59.38	45.00	1.32	51.68
8	2.5	10	15.63	25.00	0.63	3.05
9	3	9	18.75	22.50	0.83	6.51
10	3.5	11	21.88	27.50	0.80	6.92
11	5	11	31.25	27.50	1.14	20.18
12	11	17	68.75	42.50	1.62	89.95
13	4	11	25.00	27.50	0.91	10.33
14	2	8	12.50	20.00	0.63	2.44
15	3.5	9	21.88	22.50	0.97	10.34
16	4.5	10	28.13	25.00	1.13	17.80
17	6.5	15	40.63	37.50	1.08	23.84
18	2.8	11	17.19	27.50	0.63	3.36
19	12.5	24	78.73	60.00	1.30	66.23
20	3.8	10	23.44	25.00	0.94	10.30
21	4.5	12	28.13	30.00	0.94	12.36
22	5.5	16	34.38	40.00	0.86	12.69
23	13.5	19	84.38	47.50	1.78	133.11
24	2.5	7	15.63	17.50	0.89	6.23
25	13	3	81.25	75.00	1.08	47.68
26	2	7	12.50	17.50	0.71	3.19
27	10	18	62.50	45.00	1.39	60.28
28	20	35	125.00	87.50	1.43	127.57
29	7.5	14	46.88	35.00	1.34	42.04
30	2.5	11	15.63	27.50	0.57	2.53
31	36	47	225.00	117.50	1.92	412.52
32	13	18	81.25	45.00	1.81	132.44
33	6	14	37.50	35.00	1.07	21.53
34	1.5	7	9.38	17.50	0.54	1.35

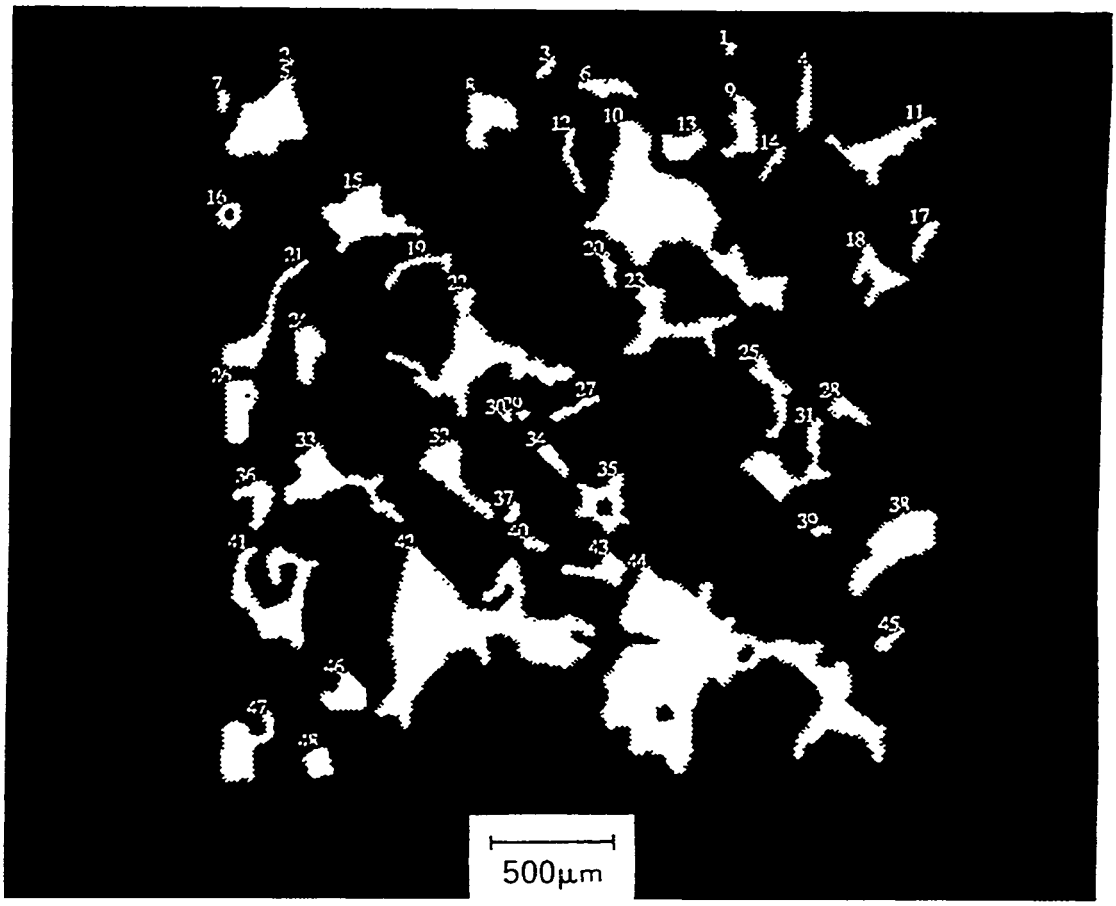

FIG. 3.7: Pore-space contours obtained from serial section of Massilon sandstone (after Koplik et al., 1984).

TABLE 3.3: Conductance data - Massilon sandstone SEM section.

N_i	A_i (units)	P_i (units)	A_i $\times 10^{-8}(\mathrm{m}^2)$	P_i $\times 10^{-4}$ (m)	R_{H_i} $\times 10^{-5}$(m)	C_i $\times 10^{-19}$ (m^4)
1	33	43	22.92	35.83	6.40	4687.54
2	54	62	37.50	51.67	7.26	9877.23
3	28	38	19.44	31.67	6.14	3665.33
4	14	36	9.72	30.00	3.24	510.50
5	8	15	5.56	12.50	4.45	548.83
6	10	14	6.94	11.67	5.95	1229.90
7	7	15	4.86	12.50	3.89	367.56
8	6	21	4.17	17.50	2.38	118.13
9	10	25	6.94	20.83	3.33	385.74
10	6	20	4.17	16.67	2.50	130.23
11	6	14	4.17	11.67	2.50	265.78
12	5	14	3.47	11.67	2.98	153.74
13	5	15	3.47	12.50	2.78	133.93
14	5	10	3.47	8.33	4.17	301.37
15	5	10	3.47	8.33	4.17	301.37
16	4	10	2.78	8.33	4.53	154.37
17	4	9	2.78	7.50	3.70	190.57
18	4	9	2.78	7.50	3.70	190.57
19	4	9	2.78	7.50	3.70	190.57
20	3	7	2.08	5.83	3.57	132.82
21	3	8	2.08	6.67	3.12	101.67
22	2	7	1.39	5.83	2.38	39.38
23	2	6	1.39	5.00	2.78	53.60
24	3	10	2.08	8.33	2.50	65.08
25	1.5	6	1.04	5.00	2.08	22.63
26	1.5	7	1.04	5.83	1.79	16.63
27	2	7	1.39	5.83	2.38	39.38
28	1.25	5	0.87	4.17	2.08	18.83
29	1.5	6	1.04	5.00	2.08	22.63
30	2	9	1.39	7.50	1.85	23.82
31	1.5	7	1.04	5.83	1.79	16.63
32	1	5	0.69	4.17	1.67	9.63
33	2	7	1.39	5.83	2.38	39.38
34	2	5	1.39	4.17	3.33	77.17
35	1	4	0.69	3.33	2.08	15.05
36	0.5	2	0.35	1.67	2.08	7.52
37	0.5	3	0.35	2.50	1.39	3.34
38	0.5	2.5	0.35	2.08	1.67	4.81
39	0.75	4	0.52	3.33	1.56	6.37
40	0.75	5	0.52	4.17	1.25	4.07
41	1	4	0.69	3.33	2.08	15.05
42	0.25	1.5	0.17	1.25	1.39	1.69
43	0.75	3	0.52	2.50	2.08	11.31
44	0.50	1.5	0.35	1.25	2.78	13.37
45	0.13	0.75	0.09	0.63	0.14	0.84
46	0.13	1	0.09	0.83	0.10	0.47
47	0.13	1	0.09	0.83	0.10	0.47
48	0.75	4	0.52	3.33	0.16	6.37

FIG. 3.8a: Typical SEM photomicrograph of Boise sandstone. The rock is composed mainly of quartz grains (dark gray). The pore space is impregnated with epoxy (black). Actual width of field is about 1 mm.

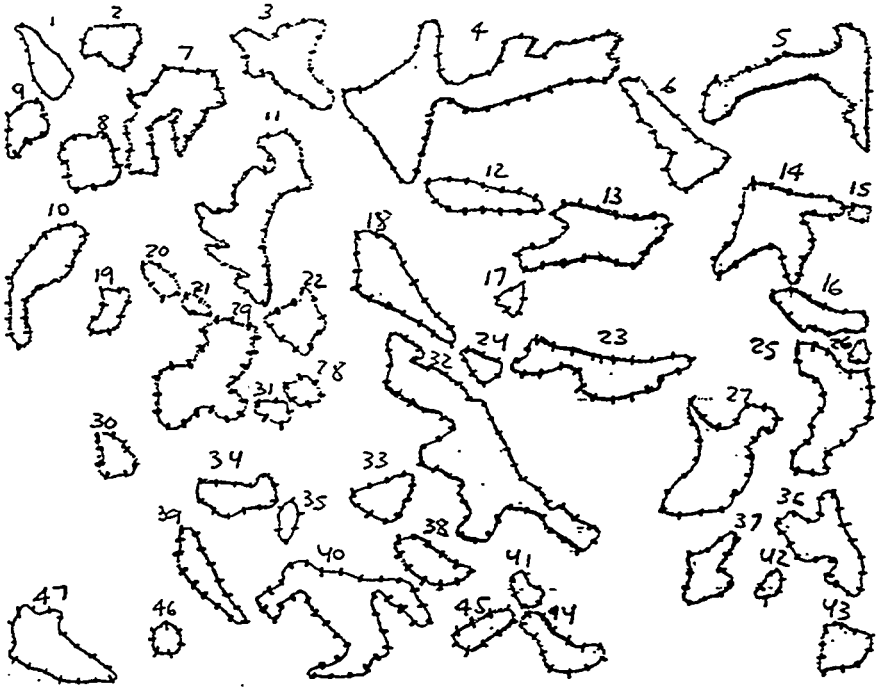

FIG. 3.8b: Pore-space contours obtained from image analysis of the photomicrograph of Boise sandstone shown in Fig. 3.8a. The width of field is about 1 mm.

TABLE 3.4: Conductance data - Boise sandstone SEM section.

N_i	A_i (units)	P_i (units)	A_i $\times 10^{-10}(\mathrm{m}^2)$	P_i $\times 10^{-4}$ (m)	R_{H_i} $\times 10^{-6}$(m)	C_i $\times 10^{-20}$ (m^4)
1	5.5	12	34.38	3.00	11.46	22.57
2	5	11	31.25	2.75	11.36	20.18
3	12.5	21	78.13	5.25	14.88	86.50
4	40	47.5	250.00	11.88	21.04	554.02
5	18	31	112.50	7.75	14.52	118.53
6	12	19.5	75.00	4.88	15.37	88.76
7	16	27	100.00	6.75	14.82	109.74
8	7	11	43.75	2.75	15.91	55.37
9	4.5	9	28.13	2.25	12.50	21.97
10	11	18	68.75	4.50	15.28	80.24
11	22	30	137.50	7.50	18.33	231.08
12	8	14.5	50.00	3.63	13.77	47.56
13	16	21	100.00	5.25	19.05	181.41
14	17	22.5	106.25	5.63	18.87	189.55
15	1	3.5	6.25	0.88	7.10	1.59
16	6	12.5	37.50	3.13	11.98	27.00
17	1.5	6	9.38	1.50	6.25	1.83
18	12	17	75.00	4.25	17.65	116.78
19	3	8	18.75	2.00	9.38	8.24
20	2	6	12.50	1.50	8.33	4.34
21	1	4	6.25	1.00	6.25	1.22
22	6	10	37.50	2.50	15.00	42.19
23	13	22	81.25	5.50	14.77	88.66
24	2.5	6.5	15.63	1.63	9.59	7.22
25	15	23	93.75	5.75	16.30	124.61
26	1	3.5	6.25	0.88	7.10	1.59
27	18	21	112.50	5.25	21.43	258.29
28	2	6	12.50	1.50	8.33	4.34
29	17.5	22	109.38	5.50	19.88	216.27
30	3.5	7.5	21.88	1.88	11.64	14.89
31	1.5	5	9.38	1.25	7.50	2.64
32	35	47	218.75	11.75	18.62	379.09
33	5	10	31.25	2.50	12.50	24.41
34	6.5	12	40.63	3.00	13.54	37.25
35	2	6.5	12.50	1.63	7.67	3.70
36	11.5	19.5	71.88	4.88	14.73	78.12
37	6.5	12	40.63	3.00	13.54	37.25
38	5.5	11	34.38	2.75	12.50	26.86
39	7	14.5	43.75	3.63	12.05	31.86
40	23.5	36.5	146.88	9.13	16.09	190.26
41	2.5	6	15.63	1.50	10.42	8.48
42	2.5	5	15.63	1.25	12.50	12.21
43	5.75	10	35.94	2.50	14.38	37.13
44	6	13	37.50	3.25	11.54	24.96
45	3.5	9	21.88	2.25	9.72	10.34
46	2	6.5	12.50	1.63	7.67	3.70
47	12.5	17	78.13	4.25	18.38	132.00

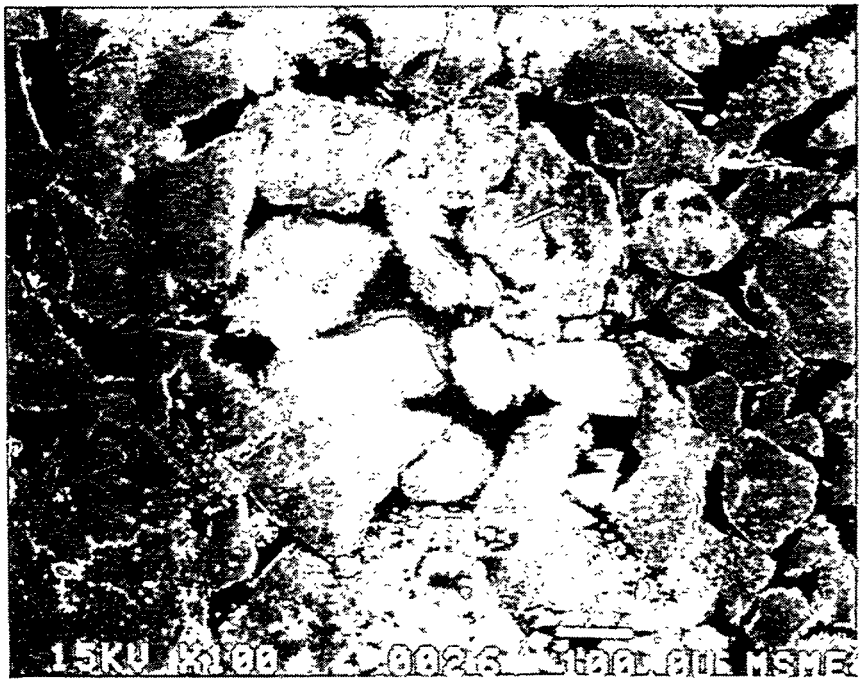

FIG. 3.9a: Typical SEM photomicrograph of Saint-Gilles sandstone. The rock is composed mainly of quartz grains (dark gray). The pore space is impregnated with epoxy (black). Actual width of field is about 1 mm.

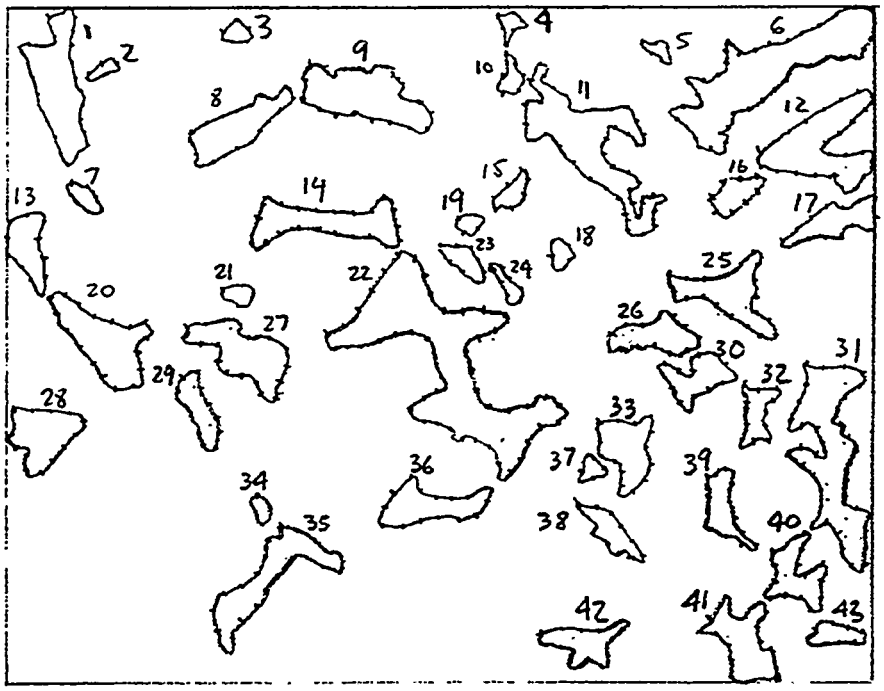

FIG. 3.9b: Pore-space contours obtained from image analysis of the photomicrograph of Saint-Gilles sandstone shown in Fig. 3.9a. The width of field is about 1 mm.

TABLE 3.5: Conductance data - Saint-Gilles sandstone SEM section.

N_i	A_i (units)	P_i (units)	A_i $\times 10^{-10}(m^2)$	P_i $\times 10^{-4}$ (m)	R_{H_i} $\times 10^{-6}$(m)	C_i $\times 10^{-20}$ (m^4)
1	13.5	25	84.38	6.25	13.50	76.89
2	1	4	6.25	1.00	6.25	1.22
3	1.5	5	9.38	1.25	7.50	263.67
4	1	6	6.25	1.50	4.17	54.25
5	1	6	6.25	1.50	4.17	54.25
6	25	38	156.25	9.50	16.45	21134.06
7	1.5	7	9.38	1.75	5.36	134.53
8	9	19	56.25	4.75	11.84	3944.12
9	14	20	87.50	5.00	17.50	13398.44
10	1.5	6.5	9.38	1.63	5.76	156.02
11	19	40.5	118.75	10.13	11.72	8167.34
12	14	24	87.50	6.00	14.58	9304.47
13	5.5	11	34.38	2.75	12.50	2685.55
14	10	21.5	62.50	5.38	11.62	4225.26
15	2	6.5	12.50	1.63	7.67	369.82
16	3	8	18.75	2.00	9.38	823.98
17	5	13.5	31.25	3.38	9.25	1339.59
18	1	4.5	6.25	1.13	5.53	96.45
19	1	4	6.25	1.00	6.25	122.07
20	12.5	17	78.13	4.25	18.38	13199.65
21	1.5	4	9.38	1.00	9.38	411.99
22	39	47	243.75	11.75	20.75	52447.91
23	2.5	8	15.63	2.00	7.82	476.84
24	1.5	7	9.38	1.75	5.36	134.53
25	9	19	56.25	4.75	11.84	3944.12
26	6	12.5	37.50	3.13	11.98	2700.00
27	11	17.5	68.75	4.38	15.70	8488.52
28	9	13.5	56.25	3.38	16.64	7812.50
29	4	12	25.00	3.00	8.33	868.06
30	6	14	37.50	3.50	10.71	2152.42
31	22	36	137.50	9.00	15.28	16046.97
32	4	12.5	25.00	3.13	7.99	800.00
33	7.5	14	46.88	3.50	13.39	4203.95
34	1	4	6.25	1.00	6.25	122.07
35	11.5	22	71.88	5.50	13.07	6137.31
36	7.5	15.5	46.88	3.88	12.08	3429.66
37	1	4	6.25	1.00	6.25	122.07
38	3.5	11	21.88	2.75	7.96	692.07
39	4.5	12	28.13	3.00	9.38	1235.96
40	6	15	37.50	3.75	10.00	1875.00
41	8.5	17	53.13	4.25	12.50	4150.39
42	5.5	14	34.38	3.50	9.82	1657.91
43	2.5	8	15.63	2.00	7.82	476.84

3.1.3 Effect of cross-sectional pore shape on permeability

As part of our analysis of the relationships between pore structure and transport properties, we have studied the effect of pore shape on permeability using the torsion analogy concept borrowed from the theory of elasticity (exact solution) and compared these results to those obtained using the hydraulic radius approximation.

3.1.3.1 *Exact solution*

There are many problems in mathematical physics which lead to the same equation and the same boundary conditions. This is the case for the analogy between the torsion of prismatic bars and the viscous flow through pipes. Thus, the general solution of the torsion problem of prismatic bars of non-circular sections will be used. The stresses are given by the relations (Sokolnikoff, 1956)

$$\tau_{xz} = Gw\frac{\partial \Psi}{\partial y}\ ;\ \ \tau_{yz} = -Gw\frac{\partial \Psi}{\partial x}\ , \tag{13}$$

where $\Psi = \Psi(x, y)$ is the stress function, G the shear modulus of elasticity, and w the angle of torsion per unit length.

If a stress function $\Psi(x, y)$ is assumed to exist such that the equations of static equilibrium are satisfied, then the equation of compatibility in a region Γ in x-y plane that the shear stresses satisfy becomes (Sokolnikoff, 1956):

$$\frac{\partial^2 \Psi}{\partial x^2} + \frac{\partial^2 \Psi}{\partial y^2} = -2\ . \tag{14}$$

The torsional rigidity is by definition,

$$D = 2G\int_{\Gamma} \Psi dA\ , \tag{15}$$

where G is the shear modulus of elasticity on A, the area of interest.

The equation of conservation of momentum or equation of motion for viscous pipe flow in a region Γ in x-y plane is (Purday, 1949)

$$\nabla^2 u(x,y) = \frac{\partial^2 u}{\partial x^2} + \frac{\partial^2 u}{\partial y^2} = \frac{1}{\mu}\frac{dp}{dz}\,, \tag{16}$$

where z is the coordinate along the axis of the tube, u is the fluid velocity in the z-direction, μ the viscosity of the fluid, and p the fluid pressure.

From the comparison of Eqs. (14) and (16) we can write

$$u = -\frac{1}{2\mu}\frac{dp}{dz}\Psi\,. \tag{17}$$

Then the continuity equation for hydraulic flux can be expressed by

$$q = \int_\Gamma u dA = -\frac{1}{2\mu}\frac{dp}{dz}\int_\Gamma \Psi dA = \frac{-D}{4\mu G}\frac{dp}{dz} = \frac{-kA}{\mu}\frac{dp}{dz}\,. \tag{18}$$

Therefore, if the torsional rigidity D of the section is calculated, the exact permeability k can be calculated.

3.1.3.2 *Hydraulic radius approximation*

According to Hagen-Poiseuille equation, the volumetric flux of fluid through a cylindrical tube of radius a is given exactly by

$$q = \frac{\pi a^4}{8\mu}\nabla p\,. \tag{19}$$

Since the area A of a circle is πa^2 and the perimeter P of a circle is $2\pi a$, then the radius a is $2A/P$. Therefore, the permeability can be expressed in terms of the hydraulic radius as

$$k = \frac{a^2}{8} = \frac{1}{8}\left(\frac{2A}{P}\right)^2 = \frac{1}{2}\left(\frac{A}{P}\right)^2 \equiv \frac{1}{2}R_H^2\,. \tag{20}$$

This equation is exact for circular cross sections. The 'hydraulic radius' method assumes that Eq. (20) can be used for all cross sections.

Now we show examples to test the equivalence of the calculated permeabilities for various pore shapes using the torsion analogy (exact solution) and the hydraulic radius approximation, respectively.

3.1.3.3 *Examples*

1. Circular shape of radius a:

   Since the area A of a circle is πa^2 and the perimeter P of a circle is $2\pi a$, then the radius a is $2A/P$.

   The permeability using the hydraulic approximation is

$$k_{circle}^{H.R.} = \frac{1}{8}\left(\frac{2A}{P}\right)^2 = \frac{a^2}{8}\,. \tag{21}$$

   The torsional rigidity D for a circular shape of radius a is (Sokolnikoff, 1956)

$$D = \frac{\pi G a^4}{2}\,. \tag{22}$$

   Thus

$$q = \frac{-\pi G a^4/2}{4\mu G}\frac{dp}{dz} = \frac{-\pi a^4}{8\mu}\frac{dp}{dz}\,. \tag{23}$$

   According to Darcy's law

$$q = -\frac{kA}{\mu}\frac{dp}{dz} = \frac{-k\pi a^2}{\mu}\frac{dp}{dz}\,, \tag{24}$$

   where k is permeability.

   Thus, the exact permeability is

$$k_{circle}^{EXACT} = \frac{\pi a^4/8}{\pi a^2} = \frac{a^2}{8}\,. \tag{25}$$

   Hence, for a circular shape

$$k_{circle}^{H.R.} \equiv k_{circle}^{EXACT}\,. \tag{26}$$

As expected then for a circular tube, the calculated permeability using the torsion analogy (exact solution) is equivalent to the permeability given by the hydraulic radius approximation.

2. Triangle of side a:

   The area A of an equilateral triangle of side a is $\sqrt{3}a^2/4$, and the perimeter P is equal to $3a$. Thus, $2A/P = \sqrt{3}a/6$.

   The permeability using the hydraulic radius approximation is

$$k_{triangle}^{H.R.} = \frac{1}{8}\left(\frac{2A}{P}\right)^2 = \frac{1}{8}\left(\frac{\sqrt{3}a}{6}\right)^2 = \frac{a^2}{96} . \tag{27}$$

   The torsional rigidity is (Berker, 1963)

$$D = \frac{\sqrt{3}Ga^4}{80} . \tag{28}$$

   The permeability using the exact solution is

$$k_{triangle}^{EXACT} = \frac{D}{4GA} = \frac{G\sqrt{3}a^4/80}{4G\sqrt{3}a^2/4} = \frac{a^2}{80} . \tag{29}$$

   Thus, the error involved in the hydraulic radius approximation is

$$ERROR = \frac{k_{triangle}^{H.R.}}{k_{triangle}^{EXACT}} = \frac{80}{96} \times 100 = -20\% . \tag{30}$$

3. Square of side a:

   The area A of a square of side a is a^2, and the perimeter P is equal to $4a$. Thus, $2A/P = a/2$.

   The permeability using the hydraulic radius approximation is

$$k_{square}^{H.R.} = \frac{1}{8}\left(\frac{2A}{P}\right)^2 = \frac{a^2}{32} . \tag{31}$$

   The torsional rigidity is (Berker, 1963)

$$D = \frac{2.253Ga^4}{16} . \tag{32}$$

The permeability using the exact solution is

$$k_{square}^{EXACT} = \frac{D}{4GA} = \frac{2.253Ga^4/16}{4Ga^2} = \frac{a^2}{28} . \tag{33}$$

Thus, the error involved in the hydraulic radius approximation is

$$ERROR = \frac{k_{square}^{H.R.}}{k_{square}^{EXACT}} = \frac{28}{32} \times 100 = -11\% . \tag{34}$$

4. Slit of length L and width h ($h \ll L$):

   The area A of a slit of length L and width h is Lh, and the perimeter $P \approx 2L$. Thus, $2A/P \approx h$.

   The permeability using the hydraulic radius approximation is

$$k_{slit}^{H.R.} = \frac{1}{8}\left(\frac{2A}{P}\right)^2 = \frac{h^2}{8} . \tag{35}$$

   The torsional rigidity is (Berker, 1963)

$$D = \frac{5.333GLh^3}{16} . \tag{36}$$

   The permeability using the exact solution is

$$k_{slit}^{EXACT} = \frac{D}{4GA} = \frac{5.333GLh^3/16}{4GLh} = \frac{h^2}{12} . \tag{37}$$

   Thus, the error involved in the hydraulic radius approximation is

$$ERROR = \frac{k_{slit}^{H.R.}}{k_{slit}^{EXACT}} = \frac{12}{8} \times 100 = +33\% . \tag{38}$$

5. Ellipse with major axis $2a$ and minor axis $2b$:

   The area A of the ellipse is πab, and the perimeter P is equal to $4aE(i)$ with $i = \sqrt{a^2 - b^2}/a$ (see elliptic integrals, Råde and Westergren, 1992). Thus, $2A/P = \pi b/2E(i)$.

   For an ellipse with $a : b = 4 : 1$, the ratio $2A/P = a/3.325$. Thus, the permeability using the hydraulic radius approximation is

$$k_{ellipse}^{H.R.} = \frac{1}{8}\left(\frac{2A}{P}\right)^2 = \frac{a^2}{88} . \tag{39}$$

The torsional rigidity is (Berker, 1963)

$$D = \frac{G\pi a^4}{68} . \tag{40}$$

The permeability using the exact solution is

$$k_{ellipse}^{EXACT} = \frac{D}{4GA} = \frac{G\pi a^4/68}{4G\pi a^2/4} = \frac{a^2}{68} . \tag{41}$$

Thus, the error involved in the hydraulic radius approximation is

$$ERROR = \frac{k_{ellipse}^{H.R.}}{k_{ellipse}^{EXACT}} = \frac{68}{88} \times 100 = -23\% . \tag{42}$$

For an ellipse with $a : b = 10 : 1$, the ratio $2A/P = a/6.366$. Thus, the permeability using the hydraulic radius approximation is

$$k_{ellipse}^{H.R.} = \frac{1}{8}\left(\frac{2A}{P}\right)^2 = \frac{a^2}{324} . \tag{43}$$

The torsional rigidity is (Berker, 1963)

$$D = \frac{G\pi a^4}{321} . \tag{44}$$

The permeability using the exact solution is

$$k_{ellipse}^{EXACT} = \frac{D}{4GA} = \frac{G\pi a^4/321}{4G\pi a^2/10} = \frac{a^2}{403} . \tag{45}$$

Thus, the error involved in the hydraulic radius approximation is

$$ERROR = \frac{k_{ellipse}^{H.R.}}{k_{ellipse}^{EXACT}} = \frac{403}{321} \times 100 = +26\% . \tag{46}$$

TABLE 3.6: List of comparative values to show equivalence of the calculated permeabilities using the torsion analogy and the hydraulic radius approximation, respectively.

Cross section		k^{EXACT}	$k^{H.R.}$	Error (%)
Circle		$a^2/8$	$a^2/8$	–
Equilateral triangle		$a^2/80$	$a^2/96$	−20
Square		$a^2/28$	$a^2/32$	−11
Slit		$h^2/12$	$h^2/8$	+33
Ellipse	$a:b=4:1$	$a^2/68$	$a^2/88$	−23
	$a:b=10:1$	$a^2/403$	$a^2/324$	+26

A list of comparative values to show equivalence of calculated permeabilities using the torsion analogy and the hydraulic radius approximation, respectively, is presented in Table 3.6. The results of this study show that the error involved in the hydraulic radius approximation lies within $\pm 30\%$. The approximation does not systematically either underpredict or overpredict the pore conductances, so that the errors will cancel, at least partially, when applied to a network of pores of different cross sections. One may reasonably conclude that the conductivity of a tubular pore is well approximated by the hydraulic radius theory.

Boussinesq expressed the hydraulic flux q in terms of a dimensionless coefficient κ defined by the relationship (Berker, 1963)

$$q = \kappa \cdot \frac{p}{\mu l} \cdot s^2 \,, \tag{47}$$

where s represents the area of the cross section under consideration. The values of the coefficients κ are (Berker, 1963)

for the circle	0.0398
for the square	0.0351
for the equilateral triangle	0.0289

Thus, we can write

$$\kappa_{circle} = 0.0398 > \kappa_{square} = 0.0351 > \kappa_{equilateral\ triangle} = 0.0289 \,. \tag{48}$$

Results of our analysis using the torsion analogy show that for cross sections of equivalent areas after normalizing permeability with respect to the equivalent circular radius a_o,

$$k_{circle} = 0.13a_o^2 > k_{square} = 0.11a_o^2 > k_{equilateral\ triangle} = 0.09a_o^2 \,, \tag{49}$$

where k is permeability.

Therefore, the permeability results obtained using the torsion analogy are in close agreement with the Boussinesq solution.

3.1.4 Effect of pore orientation

In the 2-D section under consideration, the pore cross sections are randomly oriented with respect to the directions of the channel axes. The orientation effect has been accounted for by means of the following geometrical and stereological considerations for projected images.

3.1.4.1 *Projected line*

The fundamental relationship for projected lines (Underwood, 1970) relates the mean projected length of a randomly oriented line segment to the true length.

Consider a line segment δl with one end fixed which is free to rotate in any direction described by ϕ and θ. Figure 3.10 shows one octant of the spherical surface of area $S = \pi\delta l^2/2$ generated by rotating the line segment δl.

The average projected length is

$$\overline{\delta l'} = \frac{\int_0^{\pi/2}\int_0^{\pi/2} \delta l'\, dS}{\int_0^{\pi/2}\int_0^{\pi/2} dS} = \frac{\int_0^{\pi/2}\int_0^{\pi/2} \delta l \sin\theta \delta l^2 \sin\theta d\theta d\phi}{\int_0^{\pi/2}\int_0^{\pi/2} \delta l^2 \sin\theta d\theta d\phi} \,. \tag{50}$$

We then have

$$\overline{\delta l'} = \frac{\pi}{4}\delta l \,. \tag{51}$$

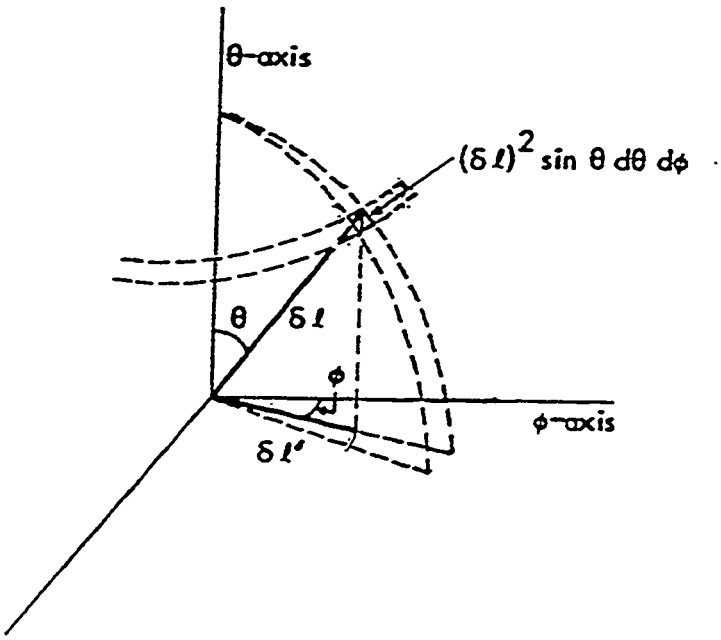

FIG. 3.10: Mean projected length of a randomly oriented linear segment (after Underwood, 1970).

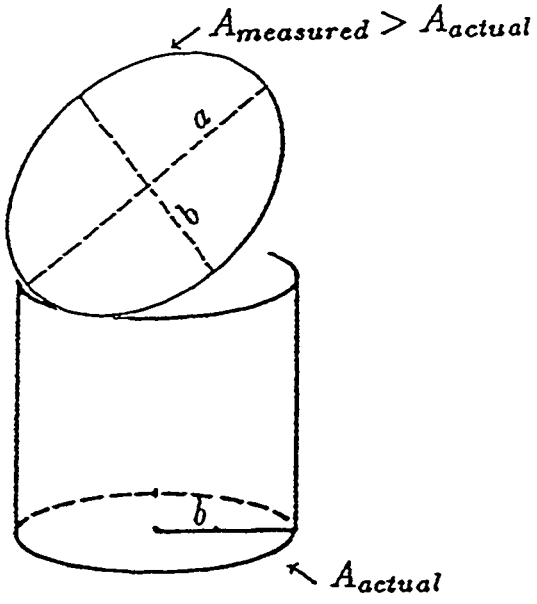

FIG. 3.11: Relationship between area of a circular tube (area actual) and its projection onto a plane (area measured).

3.1.4.2 *Projected area*

Consider a cylindrical tube of circular cross section that has been sliced by a plane oriented at an angle with respect to the channel axis (Figure 3.11). The projected cross section into the 2-D section under consideration is an ellipse with major axis $2a$, minor axis $2b$, and an area measured $A_{measured}$ equal to πab, where $a = b/\cos\theta$. The actual area of the circular section A_{actual} is equal to πb^2.

Thus we can write

$$A_{actual} = \left\langle \frac{1}{\cos\theta} \right\rangle^{-1} A_{measured} \,, \tag{52}$$

where

$$\left\langle \frac{1}{\cos\theta} \right\rangle = \frac{\int_0^{\pi} \int_0^{\theta_{max}} \frac{1}{\cos\theta} a^2 \sin\theta d\theta d\phi}{\int_0^{\pi} \int_0^{\theta_{max}} a^2 \sin\theta d\theta d\phi} \,, \tag{53}$$

with $\theta_{max} = \arctan(L/D)$, where L/D is the maximum ratio of pore length to diameter. Using an average of $L/D = 5$, as estimated from the micrographs, we find that

$$A_{actual} = 0.61 A_{measured} \,. \tag{54}$$

Evaluation of the integral appearing in Eq. (53) shows that the factor $\langle \frac{1}{\cos\theta} \rangle$ is not sensitive to the value chosen for L/D.

3.1.4.3 *Hydraulic radius*

The elliptical cross section in the 2-D section under consideration, with major axis $2a$ and minor axis $2b$, has a measured area $A_{measured}$ equal to πab, and, to within 10%, a measured perimeter $P_{measured} \approx \pi\sqrt{2(a^2+b^2)} = \pi a\sqrt{2(1+\cos^2\theta)}$ (CRC Standard Mathematical Tables, Beyer, W.H., 1988).

The measured hydraulic radius $R_{H_{measured}}$ of each tube is

$$R_{H_{measured}} \equiv \frac{A_{measured}}{P_{measured}} = \frac{\pi ab}{\pi a\sqrt{2(1+\cos^2\theta)}} \,. \tag{55}$$

The actual hydraulic radius $R_{H_{actual}}$ of each tube is

$$R_{H_{actual}} \equiv \frac{A_{actual}}{P_{actual}} = \frac{\pi b^2}{2\pi b} \,. \tag{56}$$

Thus we can write

$$R_{H_{actual}} = \frac{\sqrt{2}}{2}\left\langle \frac{1}{\sqrt{1+\cos^2\theta}} \right\rangle^{-1} R_{H_{measured}} \,, \tag{57}$$

where

$$\left\langle \frac{1}{\sqrt{1+\cos^2\theta}} \right\rangle = \frac{\int_0^{\pi}\int_0^{\theta_{max}} \frac{1}{\sqrt{1+\cos^2\theta}} a^2 \sin\theta d\theta d\phi}{\int_0^{\pi}\int_0^{\theta_{max}} a^2 sin\theta d\theta d\phi} \,. \tag{58}$$

Numerical evaluation of this integral, using $\theta_{max} = \arctan(L/D) = 78.7°$, gives

$$R_{H_{actual}} = 0.85 R_{H_{measured}} \,. \tag{59}$$

3.1.4.4 *Hydraulic conductance*

The elliptical cross section in the 2-D section under consideration, with major axis $2a$ and minor axis $2b$, has a measured area $A_{measured}$ equal to πab, and a measured perimeter $P_{measured} \approx \pi\sqrt{2(a^2+b^2)} = \pi a\sqrt{2(1+\cos^2\theta)}$.

The actual hydraulic conductance $C_{i_{actual}}$ of each tube is (aside from a length factor, which eventually cancels out of the calculations)

$$C_{i_{actual}} = \left(\frac{R_H^2}{2}A\right)_{actual} = \frac{1}{2}\left(\frac{\pi b^2}{2\pi b}\right)^2 \pi b^2 = \frac{\pi b^4}{8} \,. \tag{60}$$

The measured hydraulic conductance $C_{i_{measured}}$ of each tube from the 2-D section under consideration is (aside from a length factor, which eventually cancels out of the calculations)

$$C_{i_{measured}} = \left(\frac{R_H^2}{2}A\right)_{measured} = \frac{1}{2}\left(\frac{\pi ab}{\pi\sqrt{2(a^2+b^2)}}\right)^2 \pi ab = \frac{\pi b^4}{2\cos\theta(1+\cos^2\theta)} \,. \quad (61)$$

Thus we can write

$$(R_H^2 A)_{actual} = \frac{1}{2}\left\langle \frac{1}{\cos\theta(1+\cos^2\theta)} \right\rangle^{-1} (R_H^2 A)_{measured} \,, \quad (62)$$

where

$$\left\langle \frac{1}{\cos\theta(1+\cos^2\theta)} \right\rangle = \frac{\int_0^{\pi}\int_0^{\theta_{max}} \frac{1}{\cos\theta(1+\cos^2\theta)} a^2 \sin\theta d\theta d\phi}{\int_0^{\pi}\int_0^{\theta_{max}} a^2 \sin\theta d\theta d\phi} \,. \quad (63)$$

Numerical evaluation of this integral, using $\theta_{max} = \arctan(L/D) = 78.7°$, gives

$$(R_H^2 A)_{actual} = 0.40(R_H^2 A)_{measured} \,. \quad (64)$$

3.1.4.5 *Tortuosity and projection*

We have derived the tortuosity factor, τ, for randomly oriented cylindrical tubes in three dimensions.

According to the Hagen-Poiseuille equation, the volumetric flux of fluid through a cylindrical tube is given by (Figure 3.12)

$$q = \frac{k}{\mu}\pi b^2 \frac{\triangle p}{\triangle l} = \frac{k}{\mu}\frac{\pi ab}{\cos\theta}\frac{\triangle p}{\triangle y} \,, \quad (65)$$

where θ is the polar angle in spherical polar coordinates.

Since $b = a\cos\theta$ we get

$$\frac{\triangle p}{\triangle l}\pi b^2 = \frac{\triangle p}{\triangle y}\frac{\pi b^2}{\cos^2\theta} \,. \quad (66)$$

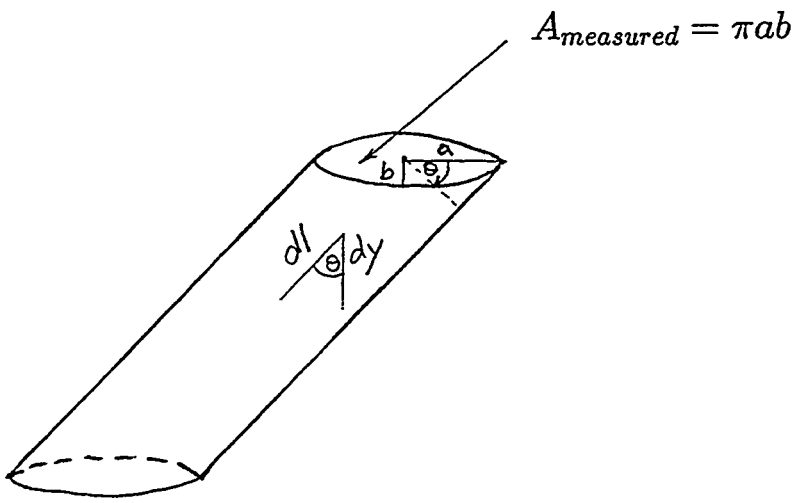

FIG. 3.12: Construction used in calculating the tortuosity factor, τ, for randomly oriented cylindrical tubes in three dimensions.

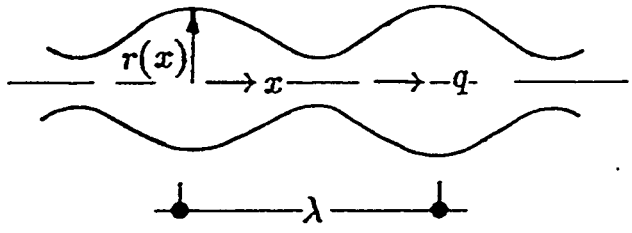

FIG. 3.13: Sinusoidal variation of the radius along the length of a tube used to calculate the constriction hydraulic factor.

We then have

$$\frac{\triangle p}{\triangle y} = \langle \cos^2 \theta \rangle \frac{\triangle p}{\triangle l} , \tag{67}$$

where

$$\langle \cos^2 \theta \rangle = \frac{\int_0^{\pi} \int_0^{\pi/2} \cos^2 \theta a^2 \sin \theta d\theta d\phi}{\int_0^{\pi} \int_0^{\pi/2} a^2 \sin \theta d\theta d\phi} = \frac{\pi/3}{\pi} = \frac{1}{3} . \tag{68}$$

Thus we can write

$$\frac{\triangle p}{\triangle y} = \frac{1}{\langle \cos^2 \theta \rangle^{-1}} \frac{\triangle p}{\triangle l} = \frac{1}{3} \frac{\triangle p}{\triangle l} , \tag{69}$$

with the tortuosity factor defined as follows:

$$\tau \equiv \langle \cos^2 \theta \rangle^{-1} = 3 . \tag{70}$$

3.1.5 Pore body to pore throat ratio dependence

Pore casts of sedimentary rocks, such as that of Berea sandstone and of Saint-Gilles sandstone (Figures 3.3 and 3.4), show that the cross section of a pore typically varies along its length. This factor must be accounted for when estimating the areas and perimeters of the pores, or else the predicted conductances will be overestimated.

We have seen that the Hagen-Poiseuille equation for the volumetric flux of fluid through a cylindrical tube is expressed as

$$q = \frac{\pi r^4}{8\mu} \nabla p . \tag{71}$$

This form of the Hagen-Poiseuille equation is valid for considering flow of water through a tube of uniform cross-sectional area. To account for the radius variation consider that for a tube of non-uniform cross-sectional area, it is more convenient to use an integral form of the Hagen-Poiseuille equation:

$$q = \frac{\pi}{8\mu} \frac{\triangle p}{\int_{x_1}^{x_2} \frac{dx}{r(x)^4}} , \tag{72}$$

in which the x axis is oriented along the flow line.

Although r may vary with x, the volumetric flowrate q must be constant across all cross sections. If Eq. (72) is written in the standard form $q = C_H \triangle p$, we find that

$$C_H = \frac{\pi}{8\mu l} \langle r^{-4} \rangle^{-1} , \tag{73}$$

where the average is taken over the length of the tube.

If we estimate from the micrograph the radius of such a tube, we will be estimating the mean value of the radius, $\langle r \rangle$, and thus will overestimate the conductance by an amount

$$\frac{C_{H_{actual}}}{C_{H_{measured}}} = \frac{\langle r^{-4} \rangle^{-1}}{\langle r \rangle^4} \equiv f , \tag{74}$$

where f is the *hydraulic constriction factor*.

The magnitude of this contriction factor will depend on the extent to which the pore radius varies. If the radius is in fact constant, then $\langle r^{-4} \rangle = \langle r \rangle^{-4}$, and $f = 1$. In order to relate f to a parameter that may be relatively simple to estimate, consider the case where the radius varies in a sinusoidal manner along the length of the tube (See Figure 3.13), according to the expression

$$r(z) = \langle r \rangle [1 + \xi \sin(2\pi x/\lambda)] , \tag{75}$$

where λ is the wavelength of the radius variations. This type of variation is supported by some pore casts, such as that of Berea sandstone shown in Figure 3.3.

For convenience, we can assume that an integral number of segments of length λ will fit into the total length l. The hydraulic constriction factor can then be expressed as

$$\frac{1}{f} = \frac{\langle r^{-4} \rangle}{\langle r \rangle^{-4}} = \frac{1}{\lambda} \int_0^{\lambda} [1 + \xi \sin(2\pi x \lambda)]^{-4} dx \, . \tag{76}$$

Using the change of variable $\varpi = 2\pi x \lambda$, the integral in Eq. (76) takes the form

$$\frac{1}{f} = \frac{1}{2\pi} \int_0^{2\pi} (1 + \xi \sin \varpi)^{-4} d\varpi \, . \tag{77}$$

With the aid of integral tables, the constriction factor f can be expressed as

$$f = \frac{256 \varrho^{7/2}}{(1+\varrho)^4 (5\varrho^3 + 3\varrho^2 + 3\varrho + 5)} \, , \tag{78}$$

where $\varrho = (1 - \xi)/(1 + \xi) = r_{min}/r_{max}$. The factor f is plotted in Figure 3.14, as a function of the parameter r_{min}/r_{max}. This factor may be as small as 0.26 for a quite reasonable value of $r_{min}/r_{max} = 0.33$ estimated from a pore cast of Saint-Gilles sandstone (See Figure 3.4). We have estimated a throat-to-pore radius ratio of 0.50 from a pore cast of Berea sandstone, and have tentatively used this value for a consolidated rock. The throat-to-pore radius aspect ratio of 0.50 for Berea sandstone is further verified by analysis on the relationship of capillary pressure of Berea sandstone to microgeometry in Chapter 5.

Although some sandstones also exhibit roughness at scales much smaller than the average pore diameter, it is known that such roughness has little effect on the hydraulic conductance (Berryman and Blair, 1987) and can therefore be ignored.

3.1.6 Permeability Calculation

Now we show how the continuum value of the hydraulic conductance is calculated. Recall that the hydraulic conductance per unit length of each tube is given by Eq. (12) as

$$C_i = \frac{1}{2} R_H^2 A \, .$$

According to the Hagen-Poiseuille equation, the volumetric flux of fluid through one tube is given by

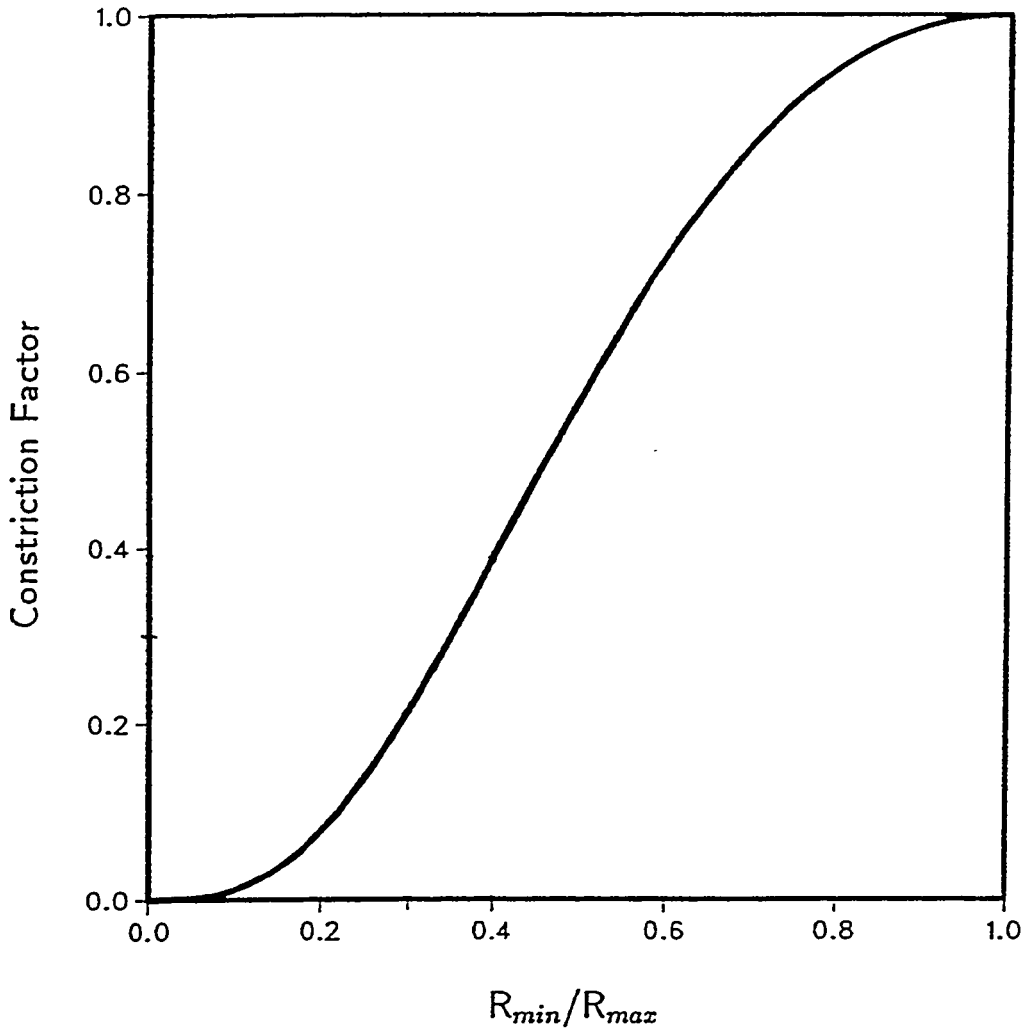

FIG. 3.14: Constriction factor for hydraulic flux as function of the ratio of the minimum pore radius to the maximum pore radius of an individual pore. The calculated conductances of the pores must be multiplied by this factor, which account for the converging-diverging nature of the pore tubes.

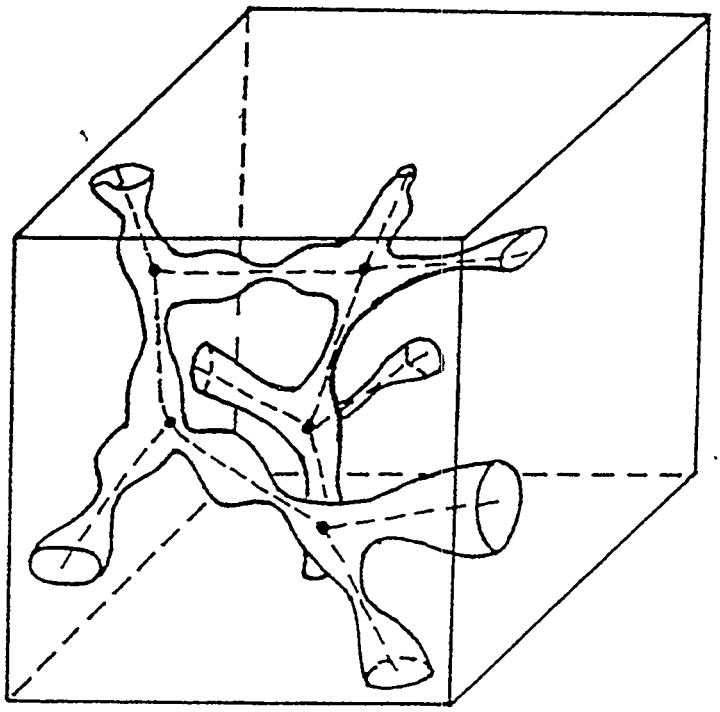

FIG. 3.15: Microscopically inhomogeneous pore system and its skeleton (after Doyen, 1988).

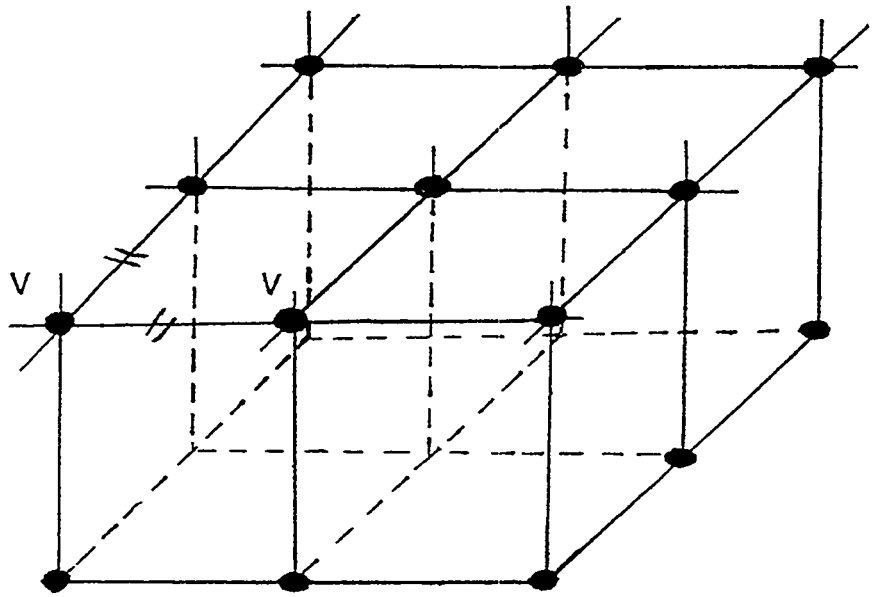

FIG. 3.16: Cubic lattice representation of the pore structure employed to calculate the permeability of sedimentary rocks with the effective medium theory.

$$q_i = \frac{C_i}{\mu} A \bigtriangledown p = \frac{R_H^2 A}{2\mu} \bigtriangledown p \,. \tag{79}$$

Study of stereo SEM photomicrographs of Berea sandstone has indicated the presence of a statistically isotropic three-dimensional pore structure represented by Figure 3.15. These observations have led to the idealization that the pores of varying size are arranged on a cubic lattice (Figure 3.16), so that the coordination number, which is the number of pores that meet at each node, is 6.

Finally, the individual conductors are imagined to be placed along the bonds of a cubic lattice in the effective medium. Recall that for a general discrete distribution of conductances, the effective medium expression (Eq. 6) takes the form

$$\sum_{i=1}^{N} \frac{C_{eff} - C_i}{[(z/2) - 1]C_{eff} + C_i} = 0 \,.$$

By solving the above equation numerically for a cubic lattice (z = 6), we have then calculated the value of the effective conductance given the individual pore conductances obtained from the SEM micrographs (See Code Listing 3.1).

In the cubic lattice, the total volumetric flux in the vertical direction is

$$q = \frac{1}{\tau} \sum_i q_{eff} = \frac{N C_{eff}}{\tau \mu} \bigtriangledown p \,, \tag{80}$$

where q_{eff} is the volumetric flux of fluid through an effective conductor and τ is the tortuosity of a cubic lattice, which is exactly equal to 3 (since one-third of the pore tubes are aligned in each of the three lattice directions).

According to the Darcy equation, the total volumetric flux through the porous medium is given by

$$q = \frac{k}{\mu} \bigtriangledown p A_{total} \,, \tag{81}$$

where k is the permeability and A_{total} is the total area of the porous medium under consideration.

Equating Eq. (80) to Eq. (81) gives the continuum value of the hydraulic conductance that is related to the effective conductance of the individual tubes:

$$k = \frac{NC_{eff}}{\tau A_{total}} . \tag{82}$$

The tortuosity for randomly oriented cylindrical tubes, $\tau \equiv \langle \cos^2 \theta \rangle^{-1} = 3$ has been derived independently (See Section 3.1.4).

3.1.7 Results and discussion

In this investigation, a network model has been developed for calculating permeability from microgeometry; this analytical model is simple, reliable, and permits accurate prediction of the laboratory measured permeability of sedimentary rocks. Calculated permeabilities for different rocks and for different coordination numbers are presented in Tables 3.7 to 3.11. A comparison between laboratory measured and predicted permeabilities with the cubic lattice-network model is given in Table 3.12. Good agreement was found between measured and predicted permeabilities for a variety of sandstones when using the cubic lattice model, with essentially no arbitrary adjustable parameters. The major conclusions that can be drawn from this study are as follows:

1. The pore structure is the most important variable influencing the permeability of sedimentary rocks.

2. The effects of the pore structure are interrelated in a complex manner with the porosity, specific surface area, and pore shape factors in the permeability analytical expression given by Eq. (82). As with the standard Kozeny-Carman model, the predicted permeability is proportional to the number of pores.

3. All the parameters in our model have an unambiguous physical meaning and are readily measured from SEM photomicrographs of rock thin sections.

TABLE 3.7: Calculated permeability data - Berea sandstone SEM section B.

z	C_{eff} (m^4)	F_s	r_{min}/r_{max}	F_c	N	A_{total} (m^2)	τ	k (m^2)	k (D)
2	4.54×10^{-20}	0.40	0.50	0.55	35	9.63×10^{-7}	3*	1.21×10^{-13}	0.12
6	18.2×10^{-20}	0.40	0.50	0.55	35	9.63×10^{-7}	3	4.84×10^{-13}	0.49
∞	56.0×10^{-20}	0.40	0.50	0.55	35	9.63×10^{-7}	3*	14.9×10^{-13}	1.51

*Assumed.

TABLE 3.8: Calculated permeability data - Berea sandstone SEM section T.

z	C_{eff} (m^4)	F_s	r_{min}/r_{max}	F_c	N	A_{total} (m^2)	τ	k (m^2)	k (D)
2	7.49×10^{-20}	0.40	0.50	0.55	35	9.84×10^{-7}	3*	1.89×10^{-13}	0.19
6	24.2×10^{-20}	0.40	0.50	0.55	35	9.84×10^{-7}	3	6.12×10^{-13}	0.62
∞	59.9×10^{-20}	0.40	0.50	0.55	35	9.84×10^{-7}	3*	15.2×10^{-13}	1.53

*Assumed.

TABLE 3.9: Calculated permeability data - Massilon sandstone SEM section.

z	C_{eff} (m^4)	F_s	r_{min}/r_{max}	F_c	N	A_{total} (m^2)	τ	k (m^2)	k (D)
2	11.7×10^{-19}	0.40	0.50	0.55	48	8.74×10^{-6}	3*	0.47×10^{-12}	0.47
6	90.7×10^{-19}	0.40	0.50	0.55	48	8.74×10^{-6}	3	3.65×10^{-12}	3.65
∞	525×10^{-19}	0.40	0.50	0.55	48	8.74×10^{-6}	3*	21.1×10^{-12}	21.1

*Assumed.

TABLE 3.10: Calculated permeability data - Boise sandstone SEM section.

z	C_{eff} (m^4)	F_s	r_{min}/r_{max}	F_c	N	A_{total} (m^2)	τ	k (m^2)	k (D)
2	8.96×10^{-20}	0.40	0.50	0.55	47	9.84×10^{-7}	3*	3.14×10^{-13}	0.32
6	45.0×10^{-20}	0.40	0.50	0.55	47	9.84×10^{-7}	3	15.8×10^{-13}	1.59
∞	80.1×10^{-20}	0.40	0.50	0.55	47	9.84×10^{-7}	3*	28.1×10^{-13}	2.83

*Assumed.

TABLE 3.11: Calculated permeability data - Saint-Gilles sandstone SEM section.

z	C_{eff} (m^4)	F_s	r_{min}/r_{max}	F_c	N	A_{total} (m^2)	τ	k (m^2)	k (D)
2	3.37×10^{-20}	0.40	0.33	0.27	43	9.84×10^{-7}	3*	1.59×10^{-13}	0.16
6	21.2×10^{-20}	0.40	0.33	0.27	43	9.84×10^{-7}	3	3.34×10^{-13}	0.34
∞	48.3×10^{-20}	0.40	0.33	0.27	43	9.84×10^{-7}	3*	7.59×10^{-13}	0.77

*Assumed.

4. When applying the method and evaluating our results one has to keep in mind that the effective medium theory is expected to work best when spatial fluctuations of hydraulic (or current) flux are small in a relative scale. In Berea sandstone for instance, our laboratory imbibition experiments in combination with SEM analysis of the pore space indicate that the distribution of pores and throats controlling permeability is narrow. Consequently, the effective medium theory is expected to and does give very good results in Berea sandstone.

5. The results given in Tables 3.7 to 3.11 emphasize the importance of pore connectivity in understanding the relationship of permeability to rock microstructure. For example, if a Kozeny-type parallel tube model ($z = \infty$) or a serial model ($z = 2$) is applied instead, permeability is overpredicted or underpredicted, respectively.

6. The investigation shows that the effective medium approximation with a parallel-tube or Kozeny-Carman arrangement with a coordination number $z = \infty$, overpredicts the measured permeability of Berea sandstone by a factor of three, and that of Massilon sandstone by a factor of six, respectively.

7. Thus, it is found that the permeability predicted with the effective medium approximation assuming a cubic lattice arrangement of the pores is consistent with the Kozeny-Carman formulas for a 'principal' pore network approaching microscopic homogeneity such as Berea sandstone's (Section 3.3.4).

8. The analysis on the effects of pore constrictivity show that permeability is controlled by connected intergranular pore throats (pore constrictions in between the grains).

9. It is found that intergranular pore throats are smaller than pore bodies, with an aspect ratio $r_{min}/r_{max} = 0.50$ for the consolidated sandstones under study.

10. For a lightly consolidated rock such as Saint-Gilles sandstone, an aspect ratio of $r_{min}/r_{max} = 0.33$ is detected. This is a direct result of the lower degree of consolidation and the more angular particle shape.

TABLE 3.12: Measured vs. predicted intrinsic permeabilities of four sedimentary rocks.

Rock	$k_{measured}$		$k_{predicted}$ ($z^a = 6$)	
	(m^2)	(d)	(m^2)	(d)
Berea sandstone	4.80×10^{-13}	0.48[b]	5.55×10^{-13}	0.56
Boise sandstone	13.0×10^{-13}	1.30[b]	15.8×10^{-13}	1.59
Massilon sandstone	25.0×10^{-13}	2.50[c]	36.5×10^{-13}	3.65
Saint-Gilles sandstone	1.70×10^{-13}	0.17[d]	3.34×10^{-13}	0.34

[a] Coordination number.

[b] Distilled water used as permeant.

[c] Data from Koplik et al., 1984.

[d] Data from Leblanc, 1988.

11. The effect of pore shape on permeability was studied by comparing the hydraulic radius approximation predictions with the exact permeabilities of various polygonal-shaped pores, and the error involved was calculated. The results of this study show that the error involved in the hydraulic radius approximation lies well within ±30% (See Table 3.6). The approximation does not systematically either underpredict or overpredict the pore conductances, so that the errors will partially cancel when applied to a network of pores of different cross sections.

12. For equivalent pore areas, Eq. (49) shows that permeability of polygonal pore shapes is not very sensitive to decreasing pore perimeter. This result is a direct consequence of the fact that the fluid velocity vanishes at the pore-grain interface. Therefore, small scale roughness is irrelevant to permeability.

3.2 Statistical approach using the perimeter-area power-law relationship of pores

Since the intrinsic permeability is a measure of the viscous resistance to fluid flow through the rock pores and is controlled by the geometry and topology of the pore space, it is expected to correlate with the amount of surface area of the pore system. In this Section, a brief discussion is given of how the perimeter-area power-law relationship of pores, along with a pore-size distribution, can be used to estimate the permeability. Consider Figure 3.17. If the outer circle has radius R_o and the inner circle (dashed line) has radius R_i, then the permeability k of a single such rough-walled cylindrical pore must satisfy (Berryman and Blair, 1984)

$$k_i \leq k \leq k_o \,, \tag{83}$$

where $k_o = R_o^4/8$, and $k_i = R_i^4/8$. If $R_o = R_i + \delta R$, then for small δR we have

$$\frac{R_i^2}{8} \leq k \leq \frac{R_i^2}{8}\left(1 + 4\frac{\delta R}{R_i}\right) \,. \tag{84}$$

In terms of hydraulic radius this can be written as

$$\frac{1}{2}\left(\frac{A_i}{P_i}\right)^2 \leq k \leq \frac{1}{2}\left(\frac{A_i}{P_i}\right)^2\left(1 + 4\frac{\delta R}{R_i}\right) \,, \tag{85}$$

where A_i and P_i are the inner tube area and perimeter, respectively.

If the surface is very rough (e.g., fractal), the pore perimeter may become so large that Eq. (85) is not satisfied. Nevertheless, it follows from Eqs. (84) and (85) that an effective hydraulic radius may be used such that

$$\left(\frac{A_i}{P_i}\right) \leq \overline{\left(\frac{A}{P}\right)} \leq \left(\frac{A_o}{P_o}\right) \,. \tag{86}$$

The parameter $\overline{(\frac{A}{P})}$ has the significance of being the hydraulic radius of a smoothed representation of the true void/solid interface. For a single straight tube (Eq. 84), if we make an error of 1% in estimating the tube radius, the error in the estimate of k

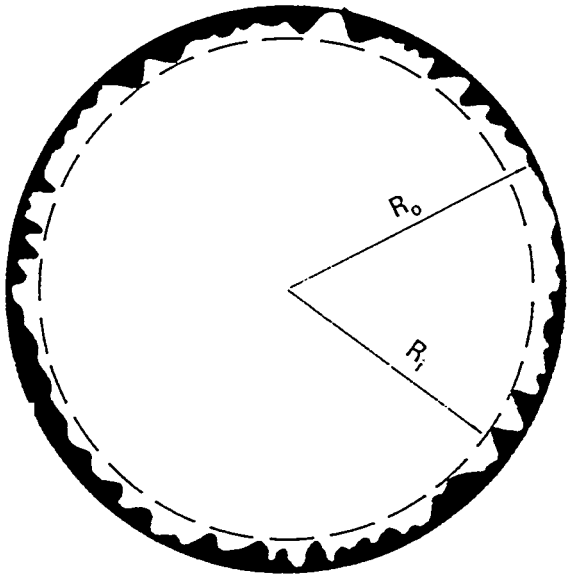

FIG. 3.17: Schematic drawing of a rough-walled tube (of radius R_o). Surface roughness does not have a strong effect on the overall fluid permeability of a tube, because a slightly smaller tube (of radius R_i) is known to have a comparable permeability (after Berryman and Blair, 1987).

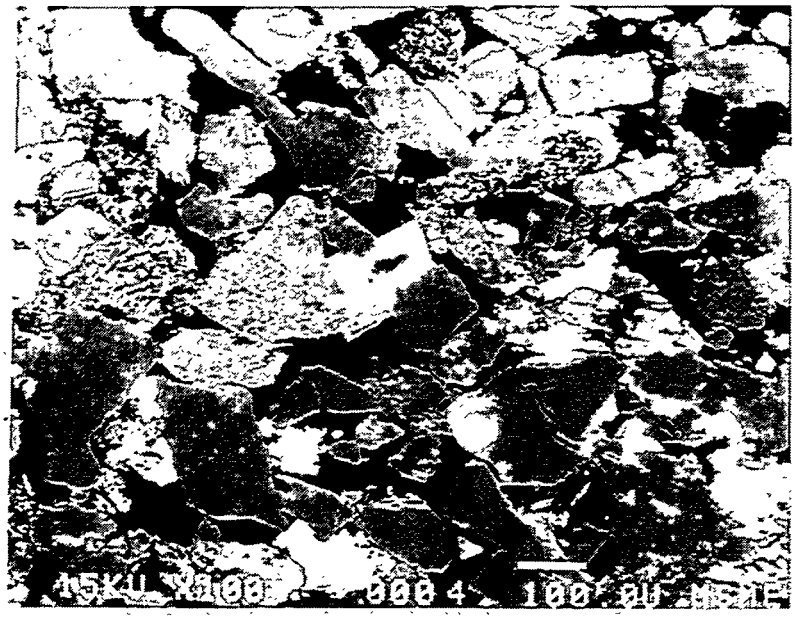

FIG. 3.18: Typical serial section of Saint-Gilles sandstone at 100x magnification. The mineral grains of different shades are quartz, carbonate, feldspar, and muscovite, whereas the darkest regions represent pore space.

TABLE 3.13. Perimeter-area power-law relationship γ parameter and correlation coefficient r measured from perimeter-area data of five sedimentary rocks.

Rock	$\phi^a_{measured}$ (%)	γ	r
Berea sandstone	22	1.49	0.99
Boise sandstone	26	1.43	0.98
Massilon sandstone	22[b]	1.43	0.98
Saint-Gilles sandstone	21	1.49	0.98
Indiana limestone	14	1.67	0.99

[a]Porosity.

[b]Data from Koplik et al., 1984.

is 4%, at worst. Indeed, since the fluid velocity vanishes at the pore-grain interface, the permeability k should not be sensitive to surface roughness.

3.2.1 Perimeter-area power-law relationship of pores

Perimeter-area relationships of a smooth representation of pores are estimated from scanning electron micrographs of thin sections of typical reservoir-type sedimentary rocks (See Figure 3.18). The basic method involves counting size and perimeter grid (or pixel) units for every feature in a standard scanning electron micrograph of some fixed magnification. The analysis was carried out using both a manual and an automated image analysis procedure to verify the accuracy of the manual technique (See Section 3.1.2 for details). The digitized thin sections (Figures 3.19a and 3.20a) then show pore space in white, and mineral grains in black. This method was used to estimate the area-perimeter statistics for a group of pores in a thin section.

It is found that the perimeter-area relationship of such a representation of the true void/solid interface satisfies the perimeter-area power-law relationship

$$A = mP^{\gamma}\,, \tag{87}$$

where $\log m$ is the intercept on the $\log A$ axis, and γ the slope of the $\log A$-$\log P$ plot (Figures 3.19b and 3.20b). The constants m and γ appearing in Eq. (87) are found by performing a linear regression on the log perimeter-log area data. From this analysis we find slopes ranging from 1.43 to 1.49 for the four sandstones examined and a slope of 1.67 for an Indiana limestone (Table 3.13).

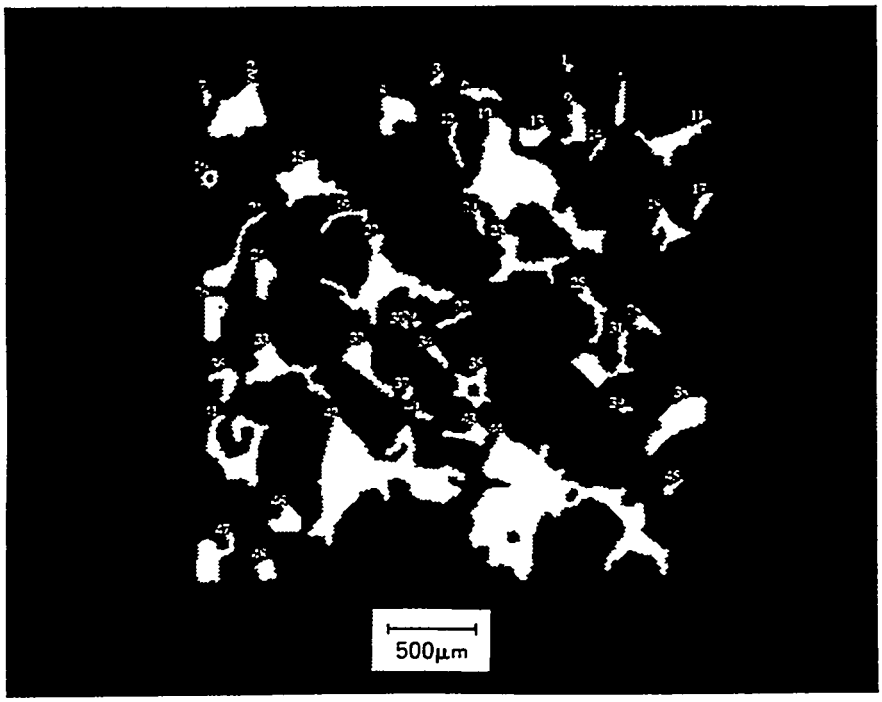

FIG. 3.19a: Pore-space contours obtained from serial section of Massilon sandstone (after Koplik et al., 1984).

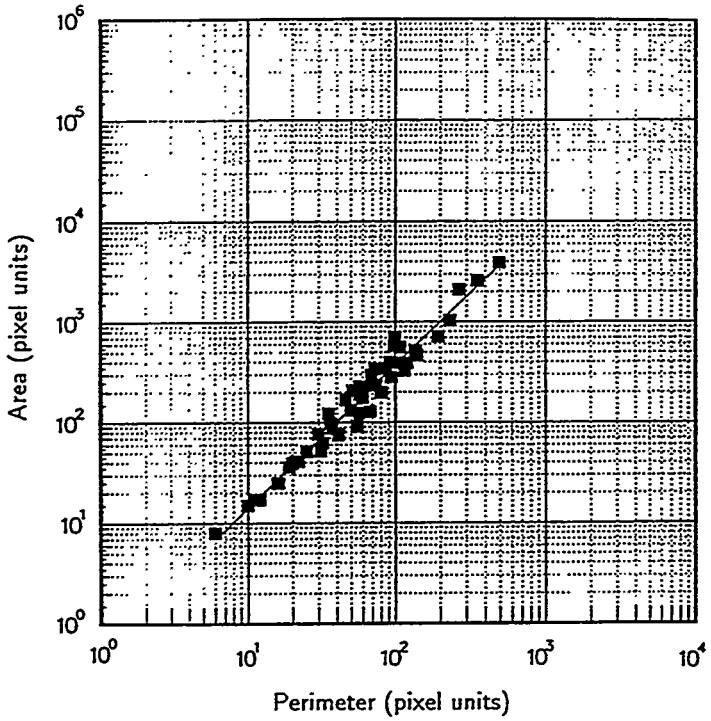

FIG. 3.19b: Perimeter-area power-law relationship for Massilon sandstone obtained from pore-space contours shown in Fig. 3.19a.

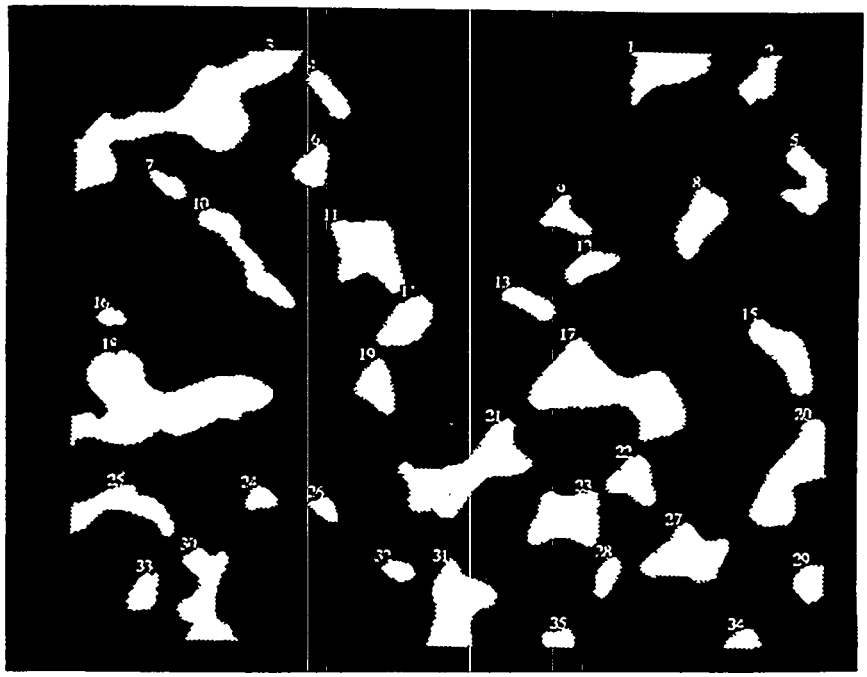

FIG. 3.20a: Pore-space contours obtained from image analysis of the photomicrograph of Berea sandstone (Section B) shown in Fig. 3.5a. The width of field is about 1 mm.

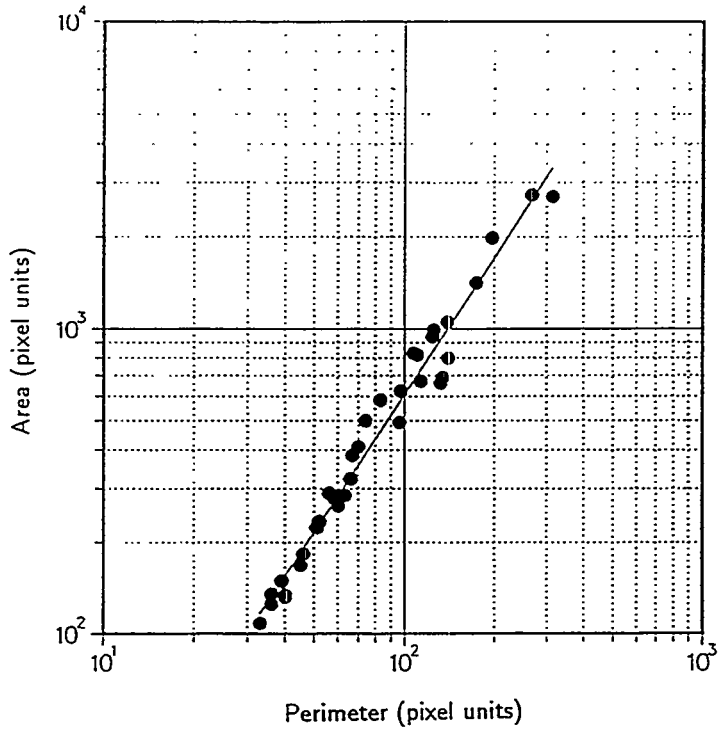

FIG. 3.20b: Perimeter-area power-law relationship of pores for Berea sandstone obtained from pore-space contours shown in Fig. 3.20a.

3.2.2 Permeability implications

We now show how the area-perimeter power-law relationship of a smoothed representation of the pore space of a rock can be used, in conjunction with a pore-size distribution and a classical model for permeability, to yield reasonable estimates of permeability. The Kozeny-Carman model for transport through a porous medium is based on the idealization of the pore space as consisting of a bundle of parallel tubes, the total conductance of which is merely the sum of the individual conductances. It is traditional to then divide this result by a tortuosity factor, $\tau = 3$, to account for the fact that, in a hydraulically isotropic rock, we would expect only one-third of the total number of tubes to be oriented in each of the three orthogonal directions (See Section 3.1.4.5 for specifics). If $n(A)$ is the number distribution function for pores of cross-sectional area A in an area of rock having total cross section of A_{total} and $C(A)$ is the conductance of each pore of area A, then the total conductance can be expressed as

$$C_{total} = \int_0^\infty n(A)C(A)dA\,. \tag{88}$$

In practice, of course, the distribution function $n(A)$ will vanish for all A greater than some A_{max}, although it is often convenient to represent $n(A)$ by a function that drops off, say, exponentially as $A \to \infty$.

If the pore tubes were all of circular cross section, their individual conductances would be given by the exact Hagen-Poiseuille law. As explained in Section 3.1.3, the Hagen-Poiseuille solution can be modified to account for irregular cross sections by using the 'hydraulic radius' approximation, which predicts a conductance of $A^3/2P^2$ for a tube of cross-sectional area A and perimeter P. Invoking the perimeter-area power-law relationship $P = m^{-1/\gamma}A^{1/\gamma}$, the hydraulic conductance can be expressed as $C(A) = A^{3-2/\gamma}/2m^{-2/\gamma}$. Combining this with the general expression (88) for the total conductance yields

$$C_{total} = \frac{1}{\tau}\int_0^\infty \frac{n(A)A^{3-2/\gamma}}{2m^{-2/\gamma}}dA\,. \tag{89}$$

We now define a normalized distribution function $\beta(A) = n(A)A/\phi A_{total}$, where

the total porosity is defined as A_{pores}/A_{total}. This distribution function has the property that $\int \beta(A)dA = 1$. The total conductance can then be expressed as

$$C_{total} = \frac{\phi A_{total}}{2m^{-2/\gamma_T}} \int_0^\infty A^{2(1-1/\gamma)} \beta(A) dA \, . \tag{90}$$

We have found that the area frequency distribution of the pores (Figures 3.21 and 3.22) can be well approximated by a lognormal distribution:

$$\hat{\beta}(u) = (2\pi\sigma_u^2)^{-1/2} \exp[-(u-u_o)^2/2\sigma_u^2] \, , \tag{91}$$

where $u = \log A$, $u_o = \log A_o$, where A_o is the most probable area, and σ_u is the variance of $\log A$. The corresponding mean area A_m is larger than the most probable area and is given by

$$A_m = A_o \exp[(\sigma_u \ln 10)^2/2] \, . \tag{92}$$

The permeability coefficient k can then be estimated as

$$\begin{aligned} k &= \frac{C_{total}}{A_{total}} = \frac{\phi}{2m^{-2/\gamma_T}} \int_0^\infty A^{2(1-1/\gamma)} \beta(A) dA \, , \\ &= \frac{\phi}{2m^{-2/\gamma_T}} A_m^{4(1-1/\gamma)^2} A_o^{2(1-1/\gamma)(2/\gamma-1)} \, . \end{aligned} \tag{93}$$

In terms of the variance of $\log A$, the permeability can be expressed as

$$k = \frac{\phi}{2m^{-2/\gamma_T}} A_m^{2(1-1/\gamma)} \exp^{-2(1-1/\gamma)(2/\gamma-1)[(\sigma_u \ln 10)^2/2]} \, . \tag{94}$$

As with the standard Kozeny-Carman model, if the pore sizes are held constant, the predicted permeability scales with the porosity, which is to say it is proportional to the number of pores. It is worth noting that if the perimeter-area relationship of the pores follows the law derived by Mandelbrot (1982) for islands whose boundaries are fractal, $P = \epsilon^D A^{D/2}$, where ϵ is some constant that depends on the length of the measuring grid size and D is the fractal dimension of the pore perimeter, then the

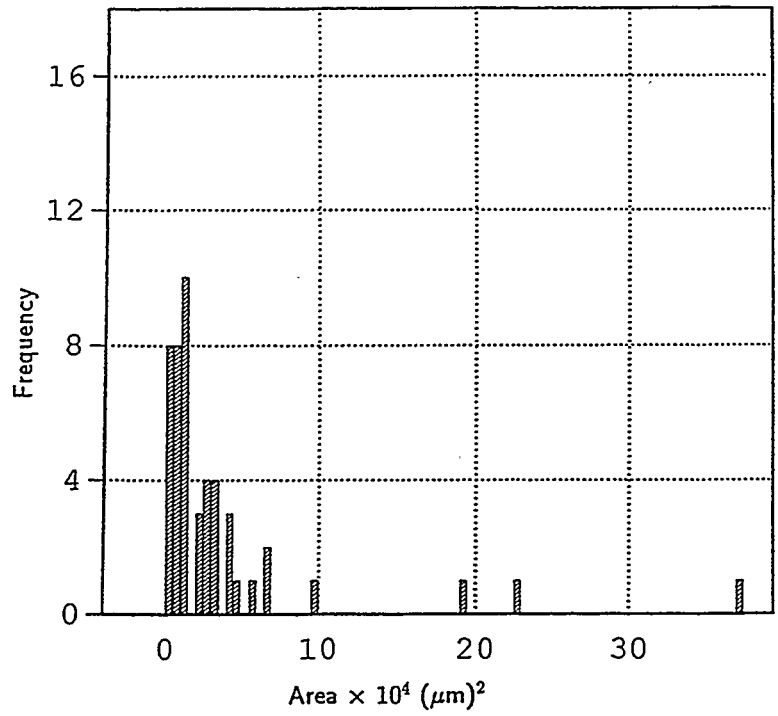

FIG. 3.21: Pore-size distribution of Massilon sandstone obtained from pore-space contours shown in Fig. 3.19a.

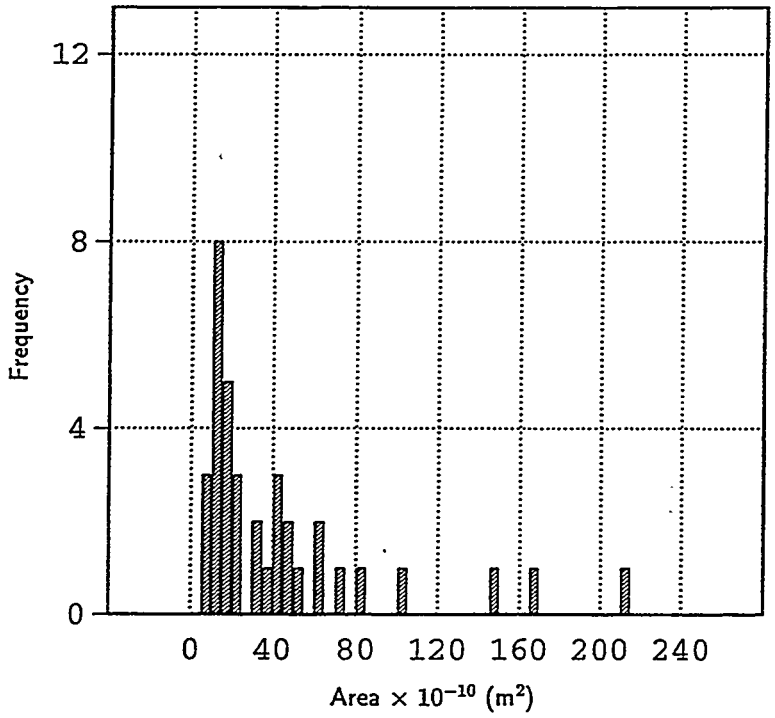

FIG. 3.22: Pore-size distribution of Berea sandstone obtained from pore-space contours shown in Fig. 3.20a.

parameter ϵ would quantify the perimeter of the pore cross sections when the pores are projected back into three dimensions. The parameter ϵ would in some sense represent the pore actual surface area, k being a decreasing function of ϵ. Therefore, if the rock pore boundaries are very rough (e.g., fractal), not only would the physical bounds for permeability be violated (Eqs. 84 and 85), but also the predicted permeabilities given by Eq. (94) would be artificially lowered by several orders of magnitude.

3.2.3 Effects of pore orientation and constrictivity

In the two-dimensional sections under consideration, the pore cross sections are randomly oriented with respect to the channel axes. The orientation effect has been taken into account by means of geometrical and stereological considerations, which indicate a stereological factor of 0.40 (See Section 3.1.4). In addition, constrictions within the individual branch channels, i.e., pore throats and bodies, have been taken into account using an analysis based on a sinusoidal variation of cross section which gives a hydraulic constriction factor of 0.55 (See Section 3.1.5).

3.2.4 Results and discussion

In this investigation, we have constructed a model that allows reasonable predictions of the permeability of sedimentary rocks, based on the perimeter-area power-law relationship of pores and the pore-size distribution. Since the permeability of rocks can range over many orders of magnitude, this prediction is not trivial. Calculated permeabilities for two different rocks are presented in Table 3.14. Image analysis of the pore system of Massilon sandstone yields values $A_m = 13.5 \times 10^4$ μm^2, $\sigma_u = 0.43$, $\gamma = 1.43$, and $m = 1.17$ μm$^{2-\gamma}$. Similarly, for Berea sandstone, $A_m = 77.9 \times 10^2$ μm^2, $\sigma_u = 0.42$, $\gamma = 1.49$, and $m = 0.66$ μm$^{2-\gamma}$. Equation (94) then predicts a permeability of 10.9 D for Massilon sandstone, and of 1.5 D for Berea sandstone, respectively (after applying the hydraulic stereological and constriction corrections) (See Table 3.14). A comparison between these results, the laboratory-measured and the predicted permeabilities with the cubic lattice-network model, is given in Table 3.15. As would be expected for an essentially parallel arrangement of conductors, as is assumed in the model, the predicted values are higher but of the same order of magnitude as the experimentally measured values of 2.5 D for Massilon sandstone (Koplik, 1984), and

TABLE 3.14: Calculated permeability data - Massilon and Berea sandstones SEM photomicrographs.

Rock	A_m (μm^2)	σ_u	γ	m (μm$^{2-\gamma}$)	F_s	F_c	τ	k (μm^2)	k (D)
Massilon	13.5×10^4	0.43	1.43	1.17	0.40	0.55	3*	10.8	10.9
Berea	77.9×10^2	0.42	1.49	0.66	0.40	0.55	3*	1.50	1.52

*Assumed.

TABLE 3.15: Measured vs. predicted intrinsic permeabilities - Massilon and Berea sandstones.

Rock	$k_{measured}$		$k_{predicted}$		$k_{predicted}$ ($z^a = 6$)	
	(m^2)	(D)	(m^2)	(D)	(m^2)	(D)
Massilon	25.0×10^{-13}	2.50[b]	108×10^{-13}	10.9	36.5×10^{-13}	3.65
Berea	4.80×10^{-13}	0.48[c]	15.0×10^{-13}	1.52	5.55×10^{-13}	0.56

[a]Coordination number.

[b]Data from Koplik et al., 1984.

[c]Distilled water used as permeant.

of 0.48 D for Berea sandstone (using distilled water as permeant) (See Table 3.15). The major conclusions that can be extracted from this study are as follows:

1. The pore structure is the most important variable influencing the permeability of sedimentary rocks.

2. Equation (94) shows that k is an increasing function of both the mean pore size and the variance of the pore size, as would be expected for an essentially parallel arrangement of conductors.

3. All the parameters in our model have an unambiguous physical meaning and are readily measured from SEM photomicrographs of rock thin sections.

4. As with the standard Kozeny-Carman model, if the pore sizes are held constant, the predicted permeability scales with the porosity, which is to say it is proportional to the number of pores.

5. Since the parameter m in Eq. (94) quantifies the perimeter of the pore cross sections, when the pores are projected back into three dimensions, m will represent the pore surface area; hence k is a decreasing function of m.

6. Our expression for k includes some length scale raised to the $2 - 2/\gamma$ power. It has a resemblance to that derived by Hansen and Skjeltorp (1988). Our result is more explicit in that our length scale is clearly identified in terms of the pore size distributions.

7. The analysis on the effects of pore constrictivity show that permeability is controlled by connected intergranular pore throats (pore constrictions in between the grains). It is found that intergranular pore throats are smaller than pore bodies, with an aspect ratio $r_{min}/r_{max} = 0.50$ for the consolidated sandstones under study.

8. Results in Table 3.15 show that the parallel-tubes statistical model overpredicts the measured permeability of Berea sandstone by a factor of three, and that of Massilon sandstone by a factor of four.

9. The parallel-tubes statistical model is consistent with the effective medium approximation and Kozeny-Carman formulas for a 'principal' pore network approaching microscopic homogeneity such as Berea sandstone's (Chapter 3.3).

10. Of course, more accurate estimates of the permeability require more sophisticated models than the parallel-tubes model, which will somehow account for factors such as the interconnectedness of the pore-tube network (See Section 3.1 and Table 3.15); the above examples were intended to be plausible demonstrations of how direct pore microgeometry measurements such as the area-perimeter power-law information, along with a pore-size distribution, can be used for making quantitative predictions of the permeability.

3.3 Note on the validity of the Kozeny-Carman formulas for consolidated porous media

The simplest and oldest capillaric model is one representing the porous medium by a bundle of parallel capillaries of uniform radius. In deriving this Kozeny-Carman model, the multiple connectivity of the pore space is completely neglected. Applying the well-known law of Hagen-Poiseuille for N circular tubes of radius r, and relating the result to the macroscopic Darcy's law, it follows that the permeability k of the bundle of capillaries is given by (Scheidegger, 1974)

$$k = \frac{N\pi\bar{r}^4}{8} = \frac{\phi\bar{r}^2}{8}\,, \tag{95}$$

where $\bar{r}$ represents an 'average' pore radius, and 'porosity' $\phi = N\pi\bar{r}^2$. This model gives permeability in one direction only. All capillaries being parallel, there can be no flow orthogonal to the capillaries. A simple modification to Eq. (95) consists of putting one-third of the capillaries in each of the three spatial dimensions. To account for this, the tortuosity factor, $\tau = 3$, is introduced, and Eq. (95) takes the form

$$k = \frac{N\pi\bar{r}^4}{8\tau} = \frac{\phi\bar{r}^2}{8\tau}\,. \tag{96}$$

The above expression for permeability can be compared with Eq. (82) which determines observed permeability of sedimentary rocks from microgeometry with reasonable accuracy (section 3.1), based on the assumption of a regular cubic lattice, consisting of pores of different shapes and varying cross sections:

$$k = \frac{NC_{eff}}{\tau A_{total}}\,.$$

If there are no marked spatial variations of the channel dimensions, the rock is microscopically homogeneous with individual conductances $C_1 = C_2 = ... = C_i = C_{eff} = C$, and the effective conductance becomes independent of the average lattice coordination number z. Therefore, under conditions of microscopic homogeneity we can write

$$k = \frac{NC_{eff}}{\tau A_{total}} = \frac{N\frac{1}{2}R_H^2 A}{\tau A_{total}} = \frac{\phi r^2}{8\tau} , \tag{97}$$

and Eq. (82) and Eq. (96) become equivalent. Indeed, the hypothesis of microscopic homogeneity of the pore space is implicit in the derivation of the Kozeny-Carman equations. This would be the case of a rock pore space characterized by a very narrow distribution of channel dimensions, e.g., a single-spike pore-size distribution or a distribution characterized by a single size. However, the pore space of a rock is generally characterized by a wide distribution of channel dimensions, and so the permeabilities predicted by the Kozeny-Carman equations deviate from the measured values. In this case, it will be shown that the Kozeny-Carman formulas based on a parallel arrangement of the pores give an upper bound on the rock permeability.

In section 3.1, a regular cubic lattice, consisting of pores of varying cross sections and different shapes, was introduced as a pore structure model. Permeabilities of sandstones obtained with this model are in good agreement with experimental data. This outcome confirms previous research by Chatzis and Dullien (1985), who found that the simple cubic (or tetrahedral) network of angular pores yields good agreement with the observed data when modeling the mercury porosimetry curve for a variety of sandstones. These results are not surprising when one notes that the above properties are strong functions of the pore structure of the sample, which is multiply connected (Figures 3.3 and 3.4). On the other hand, consider Berryman and Blair's (1986) estimates of Berea sandstone permeability using digitized SEM images of rock sections. Parameters such as porosity, specific surface area, and formation factor were employed to successfully predict permeability from Kozeny-Carman relations, and so there seems to be a discrepancy. Hence, there is a need to assess the region of validity of the Kozeny-Carman formulas to predict permeability of consolidated porous media from microgeometry, as it relates to the microscopic spatial variation of channel dimensions. It is also important to evaluate the extent to which the parallel pore structure model moves away from the regular cubic model as the pore space becomes more and more inhomogeneous at the pore scale. We undertook this research with five main objectives in mind: (1) to re-examine the effective medium theory to treat conductor networks based on the distribution of individual conductances, (2) to study the region of validity of the effective medium theory by comparing its results with con-

ductances evaluated numerically using large 3-D simple cubic networks in which the values of the conductances are chosen by a Monte Carlo procedure from one of several distributions (Kirkpatrick, 1971), (3) to compare results with the critical-path analysis (Ambegaokar et al., 1971) which focuses on the details of the critical paths along which much of the flow must occur (the total conductance obtained by this method gives an upper bound for conductivity valid for the case of a very broad distribution of channel dimensions, e.g., a microscopically heterogeneous porous medium), (4) to study the validity of the Kozeny-Carman formulas for consolidated porous media as they relate to the microscopic spatial variations of channel dimensions using the effective medium theory, network theory, and the critical path analysis, and ultimately (5) to compare the analytical results thus obtained with experimental results for a variety of consolidated porous materials.

3.3.1 Region of validity of the effective medium theory

Recall section 3.1.1 where it was shown that the average effect of a random distribution of conductances in the effective medium can be expressed by giving all conductances a single value C_{eff}, and choosing C_{eff} such that the effects of changing any conductance back to its true value will, on the average, cancel. Changing the value of a conductance located along the electric field from C_{eff} to C_o causes an additional voltage V_o to be induced across C_o given by Eq. (5),

$$V_o = \frac{V_{eff}(C_{eff} - C_o)}{C_o + (\frac{z}{2} - 1)C_{eff}} ,$$

where V_o is the voltage drop between adjacent rows far from C_o, and z, the number of bonds at each node of the network, is 6 for the simple cubic lattice employed in our model. If the conductances are distributed according to some distribution function $f(C)$, the self-consistency condition for C_{eff} is

$$0 = \langle V_o \rangle = C_{eff} \int f(C) \left[\frac{C_{eff} - C}{C + (\frac{z}{2} - 1)C_{eff}} \right] dC . \tag{98}$$

Assume a binary distribution of conductances C_{ij}, in which two values C_1 and C_2 occur with probabilities f and $1 - f$, respectively. Applying Eq. (98), we can write

$$f\frac{C_{eff}-C_1}{C_1+(\frac{z}{2}-1)C_{eff}}+(1-f)\frac{C_{eff}-C_2}{C_2+(\frac{z}{2}-1)C_{eff}}=0\,. \tag{99}$$

The following quadratic equation on C_{eff} is thus obtained:

$$\left(\frac{z}{2}-1\right)C_{eff}^2+C_{eff}\left(C_2\left[\frac{z}{2}(f-1)+1\right]+C_1\left[1-\frac{z}{2}f\right]\right)-C_1C_2=0\,. \tag{100}$$

Solving, we get

$$\begin{aligned} C_{eff} &= \frac{-C_2\left[\frac{z}{2}(f-1)+1\right]-C_1\left[1-\frac{z}{2}f\right]}{z-2} \\ &\pm \frac{\sqrt{\left(C_2\left[\frac{z}{2}(f-1)+1\right]+C_1\left[1-\frac{z}{2}f\right]\right)^2-4\left(\frac{z}{2}-1\right)C_1C_2}}{z-2}\,. \end{aligned} \tag{101}$$

Now let $C_2\rightarrow 0$, in which case C_{eff} becomes

$$C_{eff}=\frac{-C_1\left[1-\frac{z}{2}f\right]\pm C_1\left[1-\frac{z}{2}f\right]}{z-2}\,, \tag{102}$$

with solutions

$$C_{eff_1}=0\,, \tag{103}$$

and

$$C_{eff_2}=\frac{-2C_1\left[1-\frac{z}{2}f\right]}{z-2}\,. \tag{104}$$

For a simple cubic lattice, $z=6$, and the non-zero root for C_{eff} becomes

$$C_{eff}=\frac{C_1}{2}[3f-1]\,. \tag{105}$$

Thus

$$\frac{C_{eff}}{C_1} = \frac{3}{2}f - \frac{1}{2}\,. \tag{106}$$

This result is plotted in Fig. 3.23. Therefore, for $C_2 \ll C_1$, Eq. (106) predicts a linear decrease in C_{eff} with decreasing f, with $C_{eff} \to 0$ when $f \to 1/3$.

3.3.2 Numerical evaluation of the conductances of large regular 3-D networks

To study the region of validity of the effective medium theory, Kirkpatrick (1971) evaluated numerically the conductances of large regular 3-D networks, in which the simple cubic values of the conductances (the bonds of the arrays) are chosen by a Monte Carlo procedure from a distribution. The voltages V_i at the nodes of each network, and from the total current flow for a fixed external applied voltage, were calculated by a relaxation procedure based upon the Kirchhoff current law, allowing C_{eff} to be determined. If C_{ij} is the conductance of the link between adjacent nodes i and j, the condition that all currents into node i cancel is given by Eq. (1)

$$\sum_j C_{ij}(V_i - V_j) = 0\,.$$

Resistor networks give a discrete model of a continuous medium in which conductance varies with position. Kirkpatrick (1971) studied the behavior of a simple cubic network of conductances with binary disorder. The values of the conductances are 1 with probability f, and $C_2 \ll 1$ with probability $(1-f)$, assigned at random. Calculations for networks with 15^3 nodes (data points) and predictions of the effective medium theory are given for three values of C_2 in Fig. (3.23). For $C_2 \ll C_1$ the data shows a linear dependence except in the critical regions where $C_{eff}/C_1 \ll 0.1$ for the binary distribution. Hence, the effective medium theory is expected to work best when the spatial fluctuations in the current (or the channel dimensions) are relatively small. This limit leads to $C_{eff}/C_1 \to 1.0$. The opposite limit occurs when most of the current is channeled along the paths of least resistance or critical paths along which much of the current will flow. This limit leads to $C_{eff}/C_1 \to C_c$, where C_c is the critical conductance (section 3.3.3). Indeed, the effective medium theory works as long as we are not too close to f_c, the percolation limit.

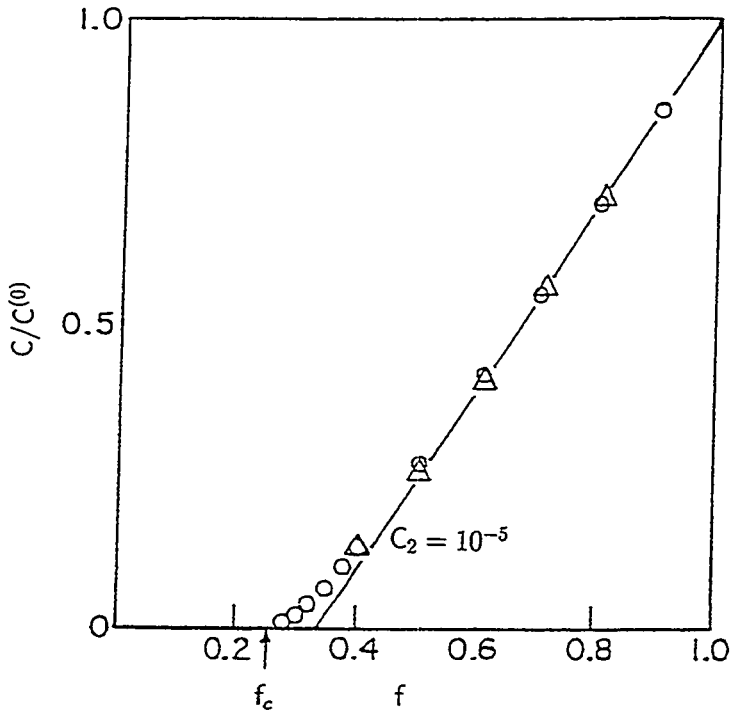

FIG. 3.23: Total conductance of a simple cubic network of conductances C_{ij} with binary disorder. Values of the conductances are 1 (with probability f) and $C_2 < 1$ (probability $1 - f$), assigned at random. Calculations for networks with 15^3 nodes (data points) and predictions of the effective medium theory (solid line) are displayed. f_c indicates the critical concentration for bond percolation on this lattice (after Kirkpatrick, 1971).

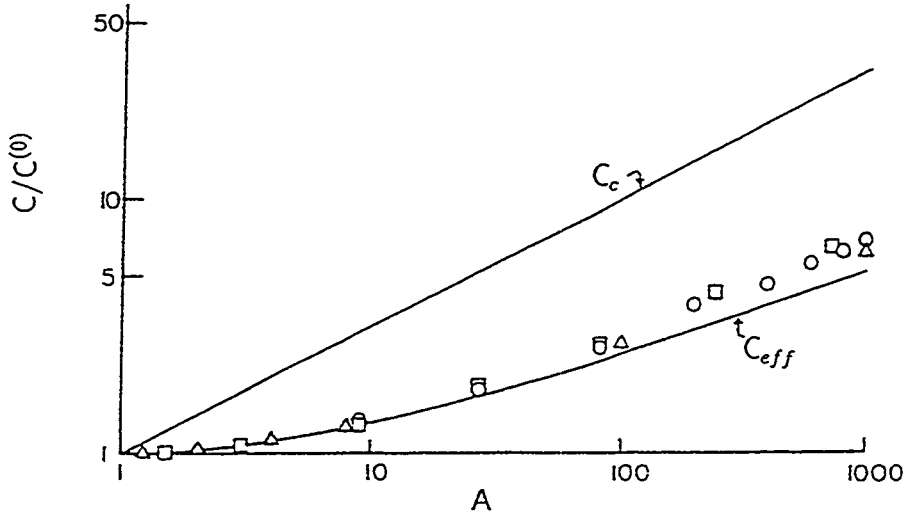

FIG. 3.24: Symbols show total conductance of a simple cubic network of 15^3 nodes, with values of the conductances chosen at random from the distribution $f(C) = (2C \log A)^{-1}$ with conductances C_{ij}'s range from A^{-1} to A. The critical path C_c and the effective conductance C_{eff} have also been plotted (after Kirkpatrick, 1971).

Kirkpatrick (1971) also calculated conductances of 3-D cubic networks of 15^3 nodes, with values of the conductances chosen at random, distributed uniformily with a distribution $f(C) = (2C \ln A)^{-1}$ and the conductances range from A^{-1} to A, and compared this result with the effective medium theory (Fig. 3.24).

3.3.3 Region of validity of the critical path analysis

Ambegaokar et al. (1971) have suggested that most of the current is channeled through the paths of least resistance at low temperatures, in inelastic hopping conduction among localized states. The localized states may be viewed as the nodes i of a random network of conductances C_{ij} with the conductance connecting any two states depending exponentially on the distance between them as well as on their energies. Ambegaokar et al. (1971) suggested that at low temperatures the conductances of such networks, and its temperature dependence, can be estimated by looking at the critical paths, and characterizing them by a critical conductance C_c. The critical conductance can be defined by a simple construction as follows. The resistance network can be considered as composed of three parts (Ambegaokar et al., 1971):

1. A set of isolated 'zones' of high conductance, each region consisting of a group of sites linked together by conductances $C_{ij} \gg C_c$.
2. A relatively small number of conductors with C_{ij} of order C_c, which connect together a subset of the high conductance clusters to form an infinite network that spans the sytem. Conductors in categories (1) and (2) are said to form the 'critical subnetwork'.
3. The remaining conductors with $C_{ij} \ll C_c$.

It is worth noting that in the critical path analysis, the conductances of order C_c determine the conductance of the network. The conductances in category (1) could all be set equal to infinity without greatly affecting the total conductance because the current has to pass through conductances of order C_c to get from one end of the system to the other. The conductances with $C_{ij} \ll C_c$ make a negligible contribution to total conductance because they are effectively shorted out by the critical subnetwork of conductors with $C_{ij} \gg C_c$. Thus the conductances are all removed from the network

and then replaced one by one, the largest first. The values of C_{ij} at which extended paths open up is C_c.

Ambegaokar et al. (1971) argue that for a very broad distribution of conductances, as is the case for low temperatures, the conductance may be expressed as

$$C \approx L^{-1} C_c \,, \tag{107}$$

where L^{-1} is less sensitive to the characteristics of the distribution of conductances than is C_c itself. Hence the temperature dependence of C is taken to be of that of C_c alone, the factor L^{-1} adding corrections of order of $\ln C_c$ or less. This analysis yields a very simple and elegant derivation of the $T^{-1/4}$ Mott law for conduction at low temperatures.

The percolation threshold, $f_c = 0.25$, of the numerical bond problem in the 3-D lattice is shown in Fig. 3.23. This value has also been reported elsewhere (Efros, 1986). If f denotes the ratio of conducting bonds to the total number of bonds, the conductance vanishing at a certain value of f is the threshold (critical) value or percolation threshold. Since $f_c = 0.25$, if the conductances are distributed uniformly over the interval (A^{-1} to A) with the weight factor $f(C) = (2C \ln A)^{-1}$, then the critical conductance C_c is easily obtained as follows:

$$f_c = \frac{\int_{C_c}^{A} f(C) d(C)}{\int_{A^{-1}}^{A} f(C) dC} = \frac{\frac{1}{2 \ln A} \int_{C_c}^{A} \frac{dC}{C}}{1} = 0.25 \;\; \Rightarrow \;\; \ln \frac{A}{C_c} = \ln A^{1/2} \,, \tag{108}$$

and

$$C_c = A^{1/2} \,. \tag{109}$$

The critical conductance for such a distribution is plotted in Fig. 3.24. For the distribution used in the calculation and for the conductances increasing up to $A \approx 1000$, this plot shows that: (1) The effective medium theory and C_{eff} for the simple cubic case only slightly underestimates the observed conductances, and (2) the conduction process is not dominated by the paths of least resistance, and the critical path analysis is immaterial.

3.3.4 Region of validity of the Kozeny-Carman formulas for consolidated porous media and the microscopic spatial variations of channel dimensions

In order to establish the validity of the Kozeny-Carman formulas for consolidated porous media, we will use the effective medium theory and assume that the conductances are distributed according to $f(C) = (2C \ln A)^{-1}$ for $A^{-1} \leq C \leq A$. The parallel ($z = \infty$) and the series ($z = 2$) arrangements will be compared to the simple cubic arrangement of the conductors ($z = 6$). In particular, the parallel arrangement (on which Kozeny-Carman formulas are based) will be compared to the simple cubic arrangement of conductors, since it was the latter that was tested with reasonable accuracy against experimental data to calculate permeability of consolidated porous media from microgeometry (Section 3.1). Also, Chatzis and Dullien (1985) have found that the simple cubic network yields results in very good agreement with the experimental data when modeling the mercury porosimetry curve for a variety of sandstones. For comparison purposes, in addition to the effective medium theory results, we plot the observed conductances obtained for a simple cubic arrangement of conductors by Kirkpatrick (1971), and the critical path analysis results in Fig. 3.25.

3.3.4.1 Parallel arrangement of the conductors

For any z we can rewrite Eq. (98) as follows

$$I = \int_{A^{-1}}^{A} \frac{dC}{2C \ln A} \left[\frac{C_{eff} - C}{\frac{C}{z} + \left(\frac{1}{2} - \frac{1}{z}\right) C_{eff}} \right] = 0 \,. \tag{110}$$

For a parallel arrangement of the conductors, $z \to \infty$, and we can write

$$I = \int_{A^{-1}}^{A} \frac{dC}{C} - \frac{1}{C_{eff}} \int_{A_{-1}}^{A} dC = 0 \,. \tag{111}$$

The two integrals can be evaluated to yield

$$\int_{A^{-1}}^{A} \frac{dC}{C} = 2 \ln A \,, \tag{112}$$

and

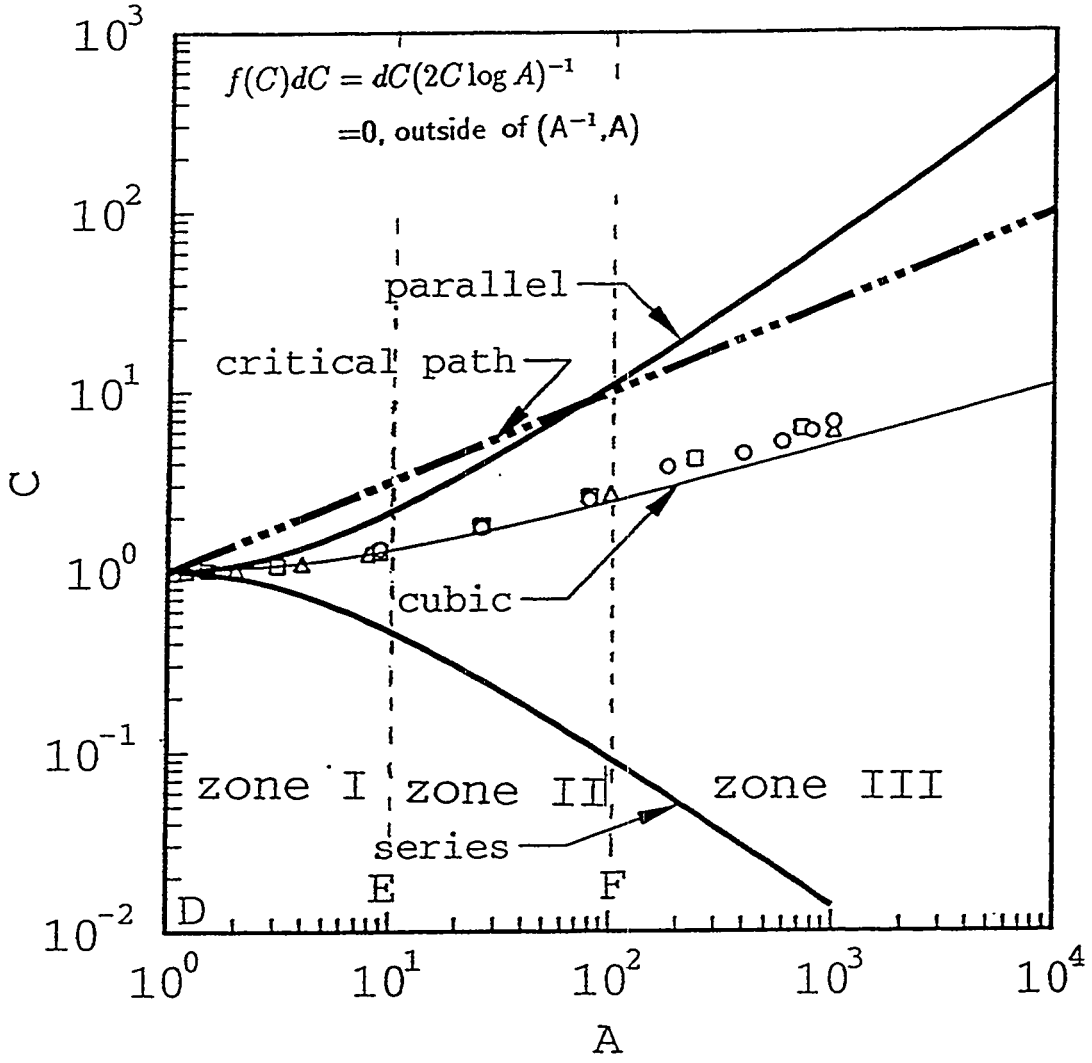

FIG. 3.25: Conductance envelope. The plot shows effective conductances of a parallel, simple cubic, and series networks of conductors, with values of the conductances chosen at random from the distribution $f(C)$ indicated. The critical path conductance and the total conductance of a simple cubic network from previous figure (data points) have also been plotted. Zones I, II, and III correspond to zones within which the Kozeny-Carman formulas are valid, approximately valid, and not valid, respectively.

$$\int_{A^{-1}}^{A} dC = \frac{A^2 - 1}{A} . \tag{113}$$

Thus, for a parallel arrangement of the conductores, C_{eff} is determined by

$$2C_{eff} \ln A = \frac{A^2 - 1}{A} . \tag{114}$$

Results are plotted in Fig. 3.25. Clearly, when $A^{-1} = A = 1$, C_{eff} becomes independent of coordination number z.

3.3.4.2 Series arrangement of the conductors

For a series arrangement of the conductors, $z = 2$, Eq. (98) gives

$$I = \int_{A^{-1}}^{A} \frac{dC}{2C \ln A} \left[\frac{C_{eff} - C}{C + \left(\frac{2}{2} - 1\right) C_{eff}} \right] = 0 . \tag{115}$$

Thus

$$I = C_{eff} \int_{A^{-1}}^{A} \frac{dC}{C^2} - \int_{A^{-1}}^{A} \frac{dC}{C} = 0 . \tag{116}$$

Solving the two integrals yields

$$\int_{A^{-1}}^{A} \frac{dC}{C^2} = \frac{A^2 - 1}{A} , \tag{117}$$

and

$$\int_{A^{-1}}^{A} \frac{dC}{C} = 2 \ln A . \tag{118}$$

Thus, for a series arrangement of the conductors, C_{eff} is determined by

$$C_{eff} \left[\frac{A^2 - 1}{A} \right] = 2 \ln A . \tag{119}$$

Results are plotted in Fig. 3.25. Clearly, as $A^{-1} = A \rightarrow 1$, C_{eff} approaches independency of coordination number z.

3.3.4.3 Simple cubic arrangement of the conductors

For a simple cubic lattice, $z = 6$, Eq. (110) gives

$$I = \int_{A^{-1}}^{A} \frac{dC}{2C \ln A} \left[\frac{C_{eff} - C}{C + \left(\frac{6}{2} - 1\right) C_{eff}} \right] = 0 \,. \tag{120}$$

Thus

$$I = \int_{A^{-1}}^{A} \frac{C_{eff} dC}{C(C + 2C_{eff})} - \int_{A^{-1}}^{A} \frac{dC}{C + 2C_{eff}} = 0 \,. \tag{121}$$

Solving the partial integrals

$$\int_{A^{-1}}^{A} \frac{C_{eff} dC}{C(C + 2C_{eff})} = -\frac{1}{2} \left[\ln \frac{2C_{eff} + A}{2C_{eff} + A^{-1}} - 2 \ln A \right] \,, \tag{122}$$

and

$$\int_{A^{-1}}^{A} \frac{dC}{C + 2C_{eff}} = \ln \frac{A + 2C_{eff}}{A^{-1} + 2C_{eff}} \,. \tag{123}$$

Thus C_{eff} for a simple cubic lattice is determined by

$$3 \ln \frac{2C_{eff} + A}{2C_{eff} + A^{-1}} = 2 \ln A \,. \tag{124}$$

Results are plotted in Fig. 3.25. Comparing the three plots (parallel, series, and cubic), as $A^{-1} = A \rightarrow 1$, C_{eff} approaches 1, irregardless of coordination number.

The solution to Eq. (123) for $A \rightarrow \infty$ is readily obtained:

$$3 \ln \frac{2C_{eff} + A}{2C_{eff}} = 3 \ln A - 3 \ln 2C_{eff} = 2 \ln A \,, \tag{125}$$

and

$$C_{eff} \approx \frac{1}{2} A^{1/3} \,. \tag{126}$$

For very large A, the data falls approximately on a straight line of slope $\sim 1/3$.

3.3.4.4 Results and discussion

Figure 3.25 shows a log-log plot of C_{eff} for the parallel, series, and the cubic arrangements, respectively. For comparison purposes, in addition to the effective medium theory results, we have plotted the critical path analysis results and the results obtained by Kirkpatrick (1971) for a simple cubic arrangement of conductors. In particular, the parallel arrangement will be compared to the simple cubic arrangement of conductors, since the latter was tested with reasonable accuracy against experimental data to calculate permeability of consolidated porous media from microgeometry (section 3.1). This result simply confirmed previous findings by Chatzis and Dullien (1985) when modeling the mercury porosimetry curve for sandstones. For the distribution used in the calculation and for the range of conductances increasing up to $A \approx 1000$, this plot shows that: (1) C_{eff} for the simple cubic case only slightly underestimates the observed conductances, (2) C_{eff} for the series case provides a lower bound for the observed conductances, (3) C_c is the uppermost bound for the observed conductances up to $A \approx 70$, whereas C_{eff} for the parallel case is the upper most bound thereafter, and (4) the conduction process is not dominated by the paths of least resistance, making the critical path analysis irrelevant.

To explore the region of validity of the Kozeny-Carman formulas, we have utilized the conductance envelope for the given distribution of conductances (Fig. 3.25), and divided it into three zones: zone I ($1 < A < 10$), a zone within which the Kozeny-Carman formulas are valid; zone II ($10 \leq A \leq 100$), a zone within which the Kozeny-Carman formulas are approximately valid within limits; and zone III ($A > 100$), a zone within which the Kozeny-Carman formulas are not valid. Zone I, in which conductance span A varies between limits 1 (point D) and 10 (point E), is characterized by conductances C_{eff} for the parallel case being less than two times higher than the cubic case over much of the conductance span. In this zone, the Kozeny-Carman relations are valid within experimental error. Consider, for exam-

ple, that in the analytical expression for permeability given by Eq. (82), the error incurred in the hydraulic radius approximation lies within ±30%. Notice that point D corresponding to the limit $A = 1 = A^{-1}$ is associated with the point at which $C_{eff} = 1$. Therefore, at point D, the porous medium is microscopically homogeneous, and the Kozeny-Carman formulas are strictly valid. In zone I, the spatial fluctuations in channel dimensions are small and the Kozeny-Carman formulas are very accurate. Notice also, that in this zone the critical path conductance C_c provides an upper most bound, and C_{eff} for the series case ($z = 2$) provides a lower bound conductance. Zone II, in which conductance span A varies between limits 10 (point E) and 100 (point F), is characterized by conductances C_{eff} for the parallel case being less than an order of magnitude higher than the simple cubic case. Since the permeability of rocks can range over many orders of magnitude, from about 10^{-11} m^2 down to about 10^{-20} m^2, an estimation of permeability within less than an order of magnitude of the observed value may be sufficient for many practical applications. However, in this zone the pore system is, strictly speaking, microscopically inhomogeneous. Zone II is a transition zone regarding the upper bound conductance because when $A \approx 80$, C_{eff} for the parallel case becomes the upper bound conductance. C_{eff} for the series case provides of a lower bound conductance during the whole span. Zone III, in which conductance span A varies between limits 100 (point F) and higher is characterized by conductances C_{eff} for the parallel case being more than order of magnitude higher than the simple cubic case. At this stage, the pore system is considered highly inhomogeneous. Notice that C_{eff} for the parallel case is here the uppermost bound. The critical path conductance, C_c, is accurate only to within an order of magnitude.

3.4 Comparison of analytical and experimental results

The analytical results for permeability calculated in the manner described above will now be (1) compared against analytical and experimental results for sandstones obtained by Chatzis and Dullien (1985), (2) compared with analytical and experimental results for sandstones obtained previously (sections 3.1 and 3.2), and (3) analyzed in light of the mercury porosimetry experimental data for a variety of sandstones obtained by Batra (1973).

As shown in section 3.1, our permeability model was able to predict the property

for a variety of sandstones while using, in every case, the same cubic lattice as the pore-structure. Chatzis and Dullien (1985) also introduced a regular cubic lattice, consisting of capillary tubes of uniform, but angular cross section, at the intersections of which are angular bulges. Drainage-type penetration numerical experiments were performed in a number of regular networks representing the pore space, using a modified site-percolation approach. All of their networks are composed of two topological entities: capillaries and nodes. The correlation between the probability of a capillary being open and that of a node being open is considered in the calculation. From these results the porosimetry curve of mercury in sandstones, the relative permeability curve of mercury in sandstones, and the relative permeability curve of oil in a sandpack were calculated. The physical basis of the calculations is a one-to-one correspondence between the probability of a capillary being open, and the cumulative distribution function of capillary diameters. Capillaries and bulges are characterized by size distribution functions, and the bulges of different sizes are distributed randomly over the nodal points (sites) of the network. The choice of the size of a capillary is limited by the condition that it may not exceed the size of either of the two bulges located at the two ends of the capillary. In the calculations, realistic capillary and node diameter distribution functions, pore shapes and relationships between the volume and the diameter of a pore were assumed. In their model, however, the aspect of the pore structure called 'geometry', such as the dimensions and the orientation of the pores, are not modeled. The cubic (or tetrahedral) network was found to give results in good agreement with the experimental data (Fig. 3.26).

The angular bonds (pore throats) correspond to pores of diameter D_b. Consistency with the customary definition of pore size used in mercury porosimetry, with the aid of the well-known relationship of Laplace, enables Chatzis and Dullien (1985) to define the capillary diameters as follows

$$D_{b_k} = 2R_{b_k} \cos\theta \,, \tag{127}$$

where R_{b_k} is the radius of curvature of the meniscus of the nonwetting phase at the prevailing capillary pressure, θ is the contact angle, and D_{b_k} is the diameter of capillary k.

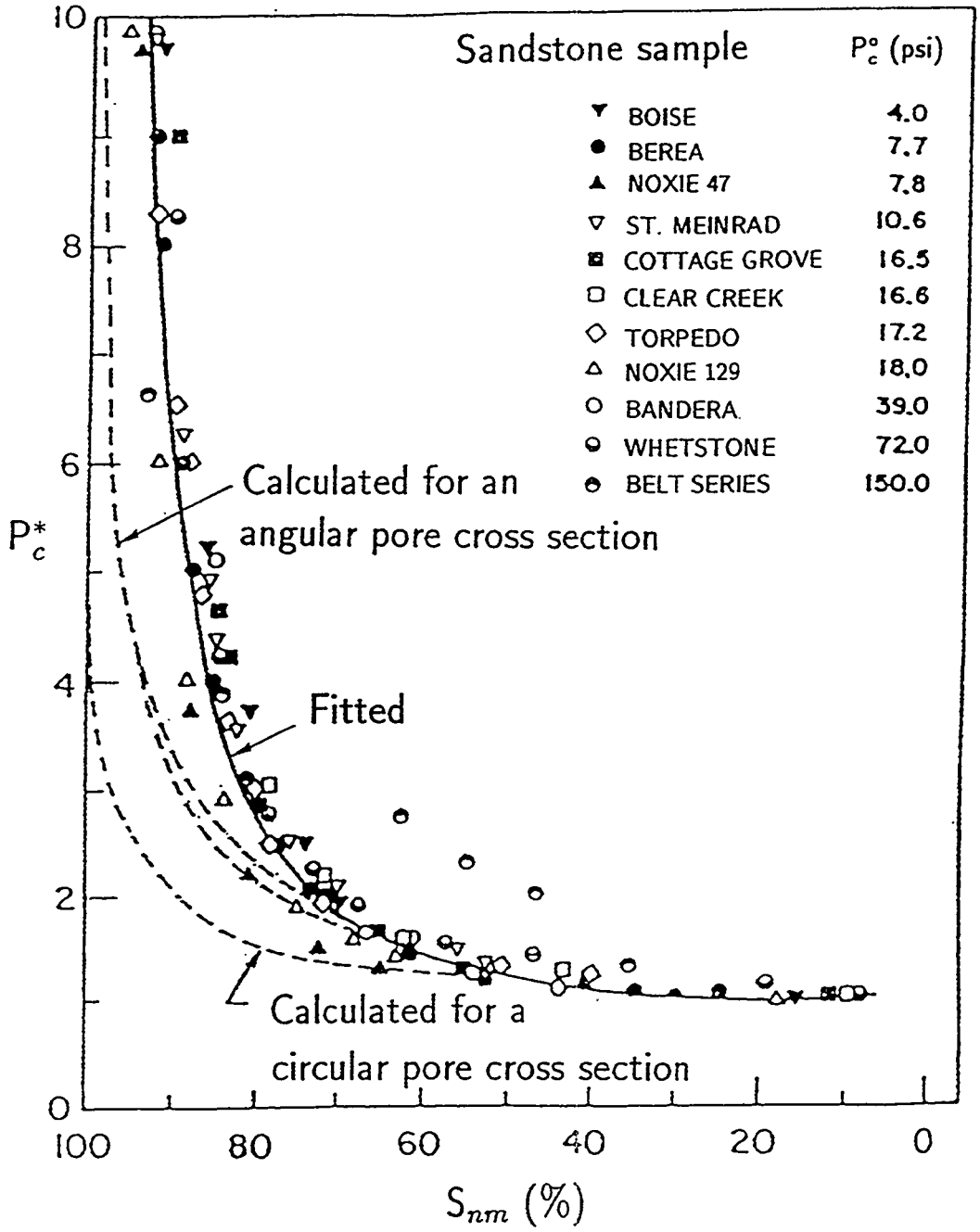

FIG. 3.26: Dimensionless experimental mercury-porosimetry data and analytical curve of sandstone samples. A regular cubic lattice consisting of capillary tubes of angular cross section, at the intersection of which there are angular bulges, is introduced as a pore structure model. The experimental data for all of the sandstone samples (except Belt Series) are well fitted by a single curve (solid line). The capillary pressure is normalized to the breakthrough capillary pressure P_c^o (after Chatzis and Dullien, 1985).

TABLE 3.16: Calculation of the mercury porosimetry curve of the Berea (BE-1) sandstone sample (after Chatzis and Dullien, 1985).

P^*_{ck}	D_{b_k}	$D^2_{b_k} f_b$	D_{s_k}	$D^2_{s_k} f_s$	S^*_{nmk}	S^o_{nmk}
1.00	29.5	102.3	44.5	848.0	0.113	0.170
1.02	28.8	104.9	44.0	843.8	0.164	0.252
1.09	27.0	109.5	42.5	826.3	0.286	0.415
1.15	25.5	110.6	41.0	802.1	0.365	0.519
1.23	24.0	109.4	39.5	771.8	0.443	0.599
1.32	22.4	105.6	38.0	735.9	0.496	0.667
1.43	20.7	99.1	37.0	709.2	0.552	0.724
1.54	19.2	91.4	35.5	665.3	0.605	0.776
1.68	17.6	81.6	34.0	617.0	0.659	0.824
1.84	16.0	70.6	33.0	582.6	0.708	0.862
2.06	14.3	58.1	31.5	527.6	0.764	0.902
2.36	12.5	44.7	30.0	468.3	0.818	0.937
2.78	10.6	31.1	28.5	403.1	0.869	0.965
3.47	8.5	17.8	27.0	327.5	0.918	0.987
5.90	5.0	0	25.0	0	0.972	1.000

Analogously, for angular nodes (pore bodies) of diameter D_{s_k}:

$$D_{s_k} = 2R_{s_k} \cos\theta \,, \tag{128}$$

where R_{s_k} is the radius of curvature of the meniscus of the nonwetting phase at the prevailing capillary pressure, θ is the contact angle, and D_{s_k} is the diameter of pore body k.

Table 3.16 (Chatzis and Dullien, 1985) gives the calculated values of the mercury porosimetry curve of the Berea (BE-1) sandstone sample using a cubic lattice of noncircular (and circular) pores. Berea (BE-1) sandstone has almost the same macroscopic transport properties as the Berea sandstone used in our experiments (i.e., porosity of 22%, permeability to N_2 of 400 mD, and a formation factor of 15.5). The capillary pressure P^*_{ck} is given relative to the breakthrough pressure P^o_c. The diameters of the pores D_{b_k}, and D_{s_k} were calculated for the prevailing capillary pressure and its corresponding saturation. The density functions $f_b(D_b)$ and $f_s(D_s)$ were assumed to be given by the beta function. The saturations $S^*_{nm_k}$ and $S^o_{nm_k}$ are the saturations of the angular and circular pore networks, respectively.

To compare our analytical calculations for permeability obtained above with the results obtained by Chatzis and Dullien (1985) for Berea (BE-1), we need first to relate the diameter D_k of each angular pore to its individual hydraulic conductance C_k (Equation 12). Schultze (1925a,b) has shown that the capillary pressures for noncircular capillaries under the assumption of zero contact angle are given by

$$P_c = \frac{\epsilon}{R_H} \; ; \quad \frac{1}{R_H} = \frac{1}{r_1} + \frac{1}{r_2} \, , \tag{129}$$

where ϵ is the surface tension, r_1 and r_2 the principal radius of curvature, and R_H the hydraulic radius as defined previously. For an equilateral triangle of side a, the equivalence of the reciprocal of the hydraulic radius and the reciprocal mean radius of curvature is (Carman, 1941)

$$\frac{1}{R_H} = \frac{1}{r_1} + \frac{1}{r_2} = \frac{2}{R_k} = \frac{4}{D_k} \, . \tag{130}$$

Thus, at zero contact angle, D_k and R_H are related. The area A and the perimeter P of the equilateral triangular pore are $\sqrt{3}a^2/4$ and $3a$, respectively. The hydraulic radius is $R_H = A/P = \sqrt{3}a/12$, and the pore diameter is $D_k = \sqrt{3}a/3$. Therefore, the angular pore area in terms of the diameter D_k is $A = 3\sqrt{3}D_k^2/4$.

Recall Eq. (12) used earlier for calculating the individual pore conductances

$$C_k = \frac{1}{2} R_H^2 A \, .$$

In terms of pore diameter D_k, and under the assumption of zero contact angle, the pore conductance becomes

$$C_k = \frac{3\sqrt{3}}{128} D_k^4 \, . \tag{131}$$

Table 3.16 (Chatzis and Dullien, 1985), gives the calculated pore diameters D_k for Berea sandstone (BE-1) for the full range of capillary pressures and saturation. At this stage, we need to calculate the pore conductances of the 'primary' pore network which is the one accountable for hydraulic transport. Our experimental results have consistently shown that the hydraulically active or 'primary' pore network in sandstones

consists of intergranular pores (bodies and throats), situated in between the grains (Chapters 4, 5, and 6). The hydraulically active or 'primary' network of intergranular pores in Berea sandstone comprises about 80% of the total rock porosity. About 20% of the total rock porosity consists of grain-contact pores; both inside the cementing material, and a few between grains when the pore has been narrowed down by deposits to a very narrow gap. Since the contribution of the grain-contact or 'secondary' network to hydraulic transport is small, it can therefore be considered hydraulically inactive (see Chapter 6). The pore (pore throat) diameters of the 'principal' network of Berea sandstone range from the critical diameter $D_c = 29.5$ μm corresponding to the breakthrough pressure P_c° (and corresponding saturation $S^*_{nm_k} = 0.113$) to the value $D_{b_k} = 12.5$ μm (and corresponding saturation $S^*_{nm_k} = 0.80$). The breakthrough diameter $D_c = 29.5$ μm is the largest diameter of the first connected cluster that spans the whole sample. On the other hand, the pore diameter $D_{b_k} = 12.5$ μm is the minimun diameter of the 'principal' network, consisting of intergranular pores, i.e., in between grains. From the 'principal' network of Berea sandstone (BE-1), the maximum and minimum pore diameters are thus obtained, and the ratio of critical to minimum pore conductances calculated with the aid of Eq. (129) is

$$\frac{C_c}{C_{min}} = \frac{D_c^4}{D_{min}^4} = \frac{29.5^4}{12.5^4} \approx 31 \,. \tag{132}$$

Using the C_c/C_{min} ratio for Berea sandstone, it is then possible to go to the general conductance plot (Fig. 3.25) and obtain the ratio of effective conductance for the parallel case ($z = \infty$) to the effective conductance for the cubic case ($z = 6$)

$$\frac{C_{eff_{parallel}}}{C_{eff_{cubic}}} \approx 3 \,. \tag{133}$$

The above result is consistent with previous calculations on permeability of Berea sandstone presented in sections 3.1 and 3.2. For example, conductance calculations for Berea sandstone section B presented in section 3.1 (Table 3.17), using the effective medium theory in conjunction with the 'principal' pore network, gave effective conductances for the parallel case ($z = \infty$) and for the cubic case ($z = 6$) such that their ratio is given by

TABLE 3.17: Calculated effective conductance data of various sandstones obtained from SEM 2-D sections (Chapter 3.1).

Rock	C_{eff} $(z^* = \infty)$ (m^4)	C_{eff} $(z^* = 6)$ (m^4)	$\frac{C_{eff}\ (z^*=\infty)}{C_{eff}\ (z^*=6)}$
Berea sandstone B	56.0×10^{-20}	18.2×10^{-20}	3.1
Berea sandstone T	59.9×10^{-20}	24.2×10^{-20}	2.5
Boise sandstone	80.1×10^{-20}	45.0×10^{-20}	1.8
Massilon sandstone	525×10^{-19}	90.7×10^{-19}	5.8
Saint-Gilles sandstone	48.3×10^{-20}	21.2×10^{-20}	2.3

*Coordinatiom number.

TABLE 3.18: Calculated permeability data of two sandstones from rock microgeometry assuming a parallel pore model (Chapter 3.2).

Rock	k $(z^* = \infty)$ (m^2)	$k_{measured}$ (m^2)	$\frac{k\ (z^*=\infty)}{k_{measured}}$
Berea sandstone B	15.0×10^{-13}	4.8×10^{-13a}	3.1
Massilon sandstone	10.8×10^{-12}	2.5×10^{-12b}	4.3

[a]Distilled water used as permeant.

[b]Data from Koplik et al., 1984.

$$\frac{C_{eff_{parallel}}}{C_{eff_{cubic}}} = \frac{56.0 \times 10^{-20}\ m^4}{18.2 \times 10^{-20}\ m^4} \approx 3\ . \tag{134}$$

Analogously, for Berea sandstone section T shown in section 3.1 (Table 3.17), the effective medium theory in conjunction with the 'principal' network gave effective conductances such that their ratio is

$$\frac{C_{eff_{parallel}}}{C_{eff_{cubic}}} = \frac{59.9 \times 10^{-20}\ m^4}{24.2 \times 10^{-20}\ m^4} \approx 3\ . \tag{135}$$

Similarly, in section 3.2 (Table 3.18), it was shown that a model based on the 'principal' pore network, a parallel arrangement, and a pore size distribution, gave the permeability for Berea sandstone section B such that its ratio to the observed value is

$$\frac{k_{parallel}}{k_{measured}} = \frac{15.0 \times 10^{-13}\ m^2}{4.8 \times 10^{-13}\ m^2} \approx 3\ . \tag{136}$$

It is then concluded that Berea sandstone hydraulically active conductances fall

into zone II of Fig. 3.25, and that the Kozeny-Carman relations are valid within a factor of three of the measured permeability values. But, how general is this result for most sandstones, especially considering that the range of pore diameters may vary widely from one rock to another? This issue becomes quite clear when one examines the normalized experimental capillary pressure curves shown in Fig. 3.26 for a variety of sandstones. They almost without exception can be represented by a single function (solid line). This is a direct consequence of the 'similarity' in the geometrical sense of the pore structure and of the 'principal' pore network of ten of the eleven sandstone samples under study. The absolute magnitudes of the pore sizes alone do not determine the results of these calculations. It is the pore diameters and pore conductances of the hydraulically active pore network, relative to the breakthrough pore diameter and corresponding conductance, rather than the absolute magnitudes of the pore diameters and corresponding conductances of the complete network, that determine the permeability and capillary pressure results. The successful prediction of permeability from microgeometry (section 3.1), and of the mercury porosimetry curve by Chatzis and Dullien (1985) of several sandstone samples, using the same cubic lattice network model as pore structure, which may appear surprising at first considering that the range of pore diameters sizes vary widely from one rock to another, becomes apparent.

Finally, it is established that the permeabilities of most sandstones fall in zone II of the conductance envelope (Fig. 3.25), and that the permeabilities predicted by the Kozeny-Carman formulas are valid within more or less a factor of three of the observed values. Consequently, even though the complete pore space system of most sandstones is strictly speaking inhomogeneous, the hydraulically active or 'principal' network approaches homogeneity. As the rock 'principal' pore network becomes more and more inhomogeneous, the conductance plot shows that the Kozeny-Carman formulas become less and less applicable. For a very inhomogeneous 'principal' network, Fig. 3.25 shows that the critical path analysis can be applied within limits.

CODE LISTING 3.1: FORTRAN source code for calculating the effective conductance given the individual conductances using the effective medium theory.

```
c**********************************************************************
c
c      Program Per: This program calculates the effective conductance in a
c                   porous medium using the effective medium approximation
c
c      created:   7/4/90   E. Schlueter
c
c      modified:  xx/xx/xx
c
c**********************************************************************
c
c     DECLARATIONS
c
      dimension hydr(5000), area(5000), peri(5000), c(5000), n(5000)
c
c**********************************************************************
c
c     INPUT DATA AND INITIALIZE
c
         open (unit=1, file='per_in.dat', status='old')
         open (unit=2, file='per_out.dat', status='old')
c
1     format(' input coon,imax')
ccc      write(5,1)
ccc      read (5,*) coon,imax
      read (1,*) coon,shfa,imax
      fact=(coon/2.)-1.
c
      do 5 i=1,imax
2        format(' input c(',i2,')')
ccc         write(5,2)i
ccc         read (5,*) c(i)
         read (1,*) j, n(i), c(i) ! j,area(i),peri(i)
c
c**********************************************************************
c
c     CALCULATIONS
c
c**********************************************************************
c
c     CALCULATION OF CONDUCTANCES
c
ccc      hydr(i)=area(i)/peri(i)
ccc      c(i)=hydr(i)*hydr(i)/shfa
5     continue
c
c**********************************************************************
c
c     CALCULATION OF MAXIMA AND MINIMA CONDUCTANCES
c
      cmax=0
      cmin=1.e6
c
      do 10 i=1,imax
         cmax=amax1(cmax,c(i))
         cmin=amin1(cmin,c(i))
10    continue
c
c**********************************************************************
c
      del_ceff=cmax-cmin
      jmax=11
      fuad=0
      ceff=cmin
```

```
      do 20 k=1,4
         del_ceff=del_ceff/10.
         do 30 j=1,jmax
c
c*************************************************************************
c
c     BISECTION LOOP
c
            ceff_old=ceff
            ceff=ceff+del_ceff
            fuad=sum(ceff,c,fact,imax,n)
c
            if(fuad .gt. 0.) then
               ceff=ceff_old
               go to 20
            endif
c
30       continue
20    continue
c
c*************************************************************************
c
c     FORMAT STATEMENTS
c
101      format('EFFECTIVE INTRINSIC PERMEABILITY CALCS.'//,
     &      'coon = ', e9.3, '   shfa = ', f9.3, '   ceff = ', f10.3,
     &      '[m*m]', /)
c102      format(xxx,...
c
c*************************************************************************
c
c     WRITE OUTPUT DATA
c
      write(5,6) ceff
6     format(' ceff = ',f10.3)
      write(2,101) coon,shfa,ceff
c
      close (unit=1, status='keep')
      close (unit=2, status='keep')
      end
c
c*************************************************************************
c
c     CALCULATION OF EFFECTIVE CONDUCTANCES
c
      function sum(ceff,c,fact,imax,n)
      dimension c(5000), n(5000)
      sum=0
c
      do 50 i=1,imax
         do 45 k=1,n(i)
         func=(ceff-c(i))/(fact*ceff+c(i))
         sum=sum+func
45       continue
50    continue
c
      return
      end
c
c*************************************************************************
```

References

[1] Ambegaokar, V., Halperin, B.I., and Langer, J.S. 1971. Hopping conductivity in disordered systems. Phys. Rev. B, 4(8), p. 2612.

[2] Batra, V.K. 1973. An experimental investigation of the structure of porous media and its relation to oil recovery. Ph.D. Thesis. University of Waterloo, Canada.

[3] Berker, R. 1963. Integration des equations du mouvement d'un fluid visqueux incompressible. Handbuch der Physik, 8(2), p. 1. Springer-Verlag, Berlin.

[4] Berryman, J.G., and Blair, S.C. 1987. Kozeny-Carman relations and image processing methods for estimating Darcy's constant. J. Appl. Phys., 62(6), p. 2221.

[5] Beyer, W.H. 1988. CRC Standard Mathematical Tables 28th Edition. CRC Press, Inc. Boca Raton, Florida.

[6] Carman, P.C. 1941. Capillary rise and capillary movement of moisture in fine sands. Soil Sci., 52, p. 1. SPEJ, April, p. 311.

[7] Chatzis I., and Dullien, F.A.L. 1985. The modeling of mercury porosimetry and the relative permeability of mercury in sandstones using percolation theory. A.I.Ch.E., 25(1), p. 47.

[8] Doyen, P. 1988. Permeability, conductivity, and the geometry of sandstone. J. Geophys. Res., 93(B7), p. 7729.

[9] Dullien, F.A.L. 1979. Porous Media Fluid Transport and Pore Structure. Academic Press.

[10] Efros, A.L. 1986. Physics and Geometry of Disorder. Mir publishers, Moscow.

[11] Hansen, J.P., and Skjeltorp, A.T. 1988. Fractal pore space and rock permeability implications. Phys. Rev. B, 38(4), p. 2635.

[12] Kirkpatrick, S. 1971. Classical transport in disordered media: Scaling and effective-medium theories. Phys. Rev., 27(25), p. 1722.

[13] Kirkpatrick, S. 1973. Percolation and conduction. Rev. Mod. Phys., 45(4), p. 574.

[14] Kirkpatrick, S. 1979. Models of disordered materials. Edité par Roger Balian, Roger Maynard, Gerard Toulouse. La Matière Mal Condensée. Ill-Condensed Matter. North Holland Publishing Company, Amsterdam-New York-Oxford.

[15] Koplik, J., Lin, C., and Vermette, M. 1984. Conductivity and permeability from microgeometry. J. of Appl. Phys., 56(11), p. 3127.

[16] Leblanc, M. 1988. Institut Francais du Petrole. Division Géologie. Gaz de France. Direction des Etudes et Techniques Nouvelles. Départment "Réservoirs Souterrains". Nos Réf.: M.D5-LM/DT-G1036.

[17] Mandelbrot, B.B. 1982. The Fractal Geometry of Nature. Freeman, San Francisco.

[18] Purday, H.F.P. 1949. Streamline Flow. Constable & Company, London.

[19] Råde, L., Westergren, B. 1990. Mathematics Handbook. CRC Press, Boca Raton, Florida.

[20] Scheidegger, A.E. 1974. The Physics of Flow through Porous Media. University of Toronto Press.

[21] Schlueter, E.M. 1995. Predicting the Transport Properties of Sedimentary Rocks from Microstructure. Ph.D. Thesis. University of California at Berkeley.

[22] Schultze, K. 1925a. Kapillarität, verdunstung, und auswitterung. Kolloid Ztschr., 36, p. 65.

[23] Schultze, K. 1925b. Kapillarität und benetzung. Kolloid Ztschr., 37, p. 10.

[24] Sokolnikoff, I.S. 1956. Mathematical Theory of Elasticity. Mc.Graw-Hill, New York.

[25] Underwood, E.E. 1970. Quantitative Stereology. Addison-Wesley, Reading, Massachusetts.